Intra- and Interband Transfers in the B800−B850 Antenna of *Rhodospirillum molischianum*: Redfield Theory Modeling of Polarized Pump−Probe Kinetics

Vladimir Novoderezhkin,[†] Markus Wendling,[‡] and Rienk van Grondelle*,[‡]

A. N. Belozersky Institute of Physico-Chemical Biology, Moscow State University, Leninskie Gory, 119992, Moscow, Russia, and Department of Biophysics and Physics of Complex Systems, Faculty of Sciences, Vrije Universiteit, De Boelelaan 1081, 1081 HV Amsterdam, The Netherlands

We use an exciton model for the B800−B850 LH2 light-harvesting antenna of *Rhodospirillum molischianum* to explain the absorption, excitation-wavelength-dependent pump−probe kinetics, and induced absorption anisotropy at 77 K reported previously (Wendling, M.; van Mourik, F.; van Stokkum, I. H. M.; Salverda, J. M.; Michel, H.; van Grondelle, R. Low-intensity pump−probe measurements on the B800 band of *Rhodospirillum molischianum. Biophys. J.* **2003**, *84*, 440). The nonlinear response was calculated using the density matrix equation, expanded up to the third-order with respect to the external field, with the Redfield relaxation operator in the exciton basis. The model allowed us to obtain a simultaneous and quantitative fit of the data while taking into account the excitonic interactions, the static disorder, and phonon-induced relaxation of populations and coherences in the one-exciton manifold (including a nonsecular coherence transfer and population-coherence coupling). The spectral density of the exciton−phonon coupling adjusted from the fit allowed us to determine the time scales and pathways of energy transfer. The 800 nm band consists of exciton states of the outer ring (B800 states) together with the upper Davydov component of the inner ring (B850* states). The 850 nm band contains the lower Davydov states of the inner ring (B850 states). The excitation dynamics includes migration around the outer ring with 1−3 ps time constant (the B800 → B800 transfer), 1 ps transfer to the inner ring (B800 → B850 transfer), and 600−800 fs transfer to higher states of the inner ring (B800 → B850* transfer). The dynamics of B850* states is characterized by very fast 100−200 fs intraband (B850* → B850*) equilibration, 60−200 fs interband (B850* → B850) relaxation, and a slower (>250 fs) back (B850* → B800) transfer. The relative contribution of the B800 → B850* → B850 pathway is comparable (approximately equal) to the contribution of the direct B800 → B850 transfer. Both B800 → B800 and B800 → B850* transfers are faster for the blue side of the 800 nm band, giving rise to slower kinetics when the excitation wavelength is tuned from 788 to 800 nm. From 800 to 809 nm kinetics become faster due to the increasing contribution of the directly excited B850* states and due to better coupling (faster relaxation) to higher states of the B850 band. The anisotropy decay in the 800 nm region exhibits a fast component (300−500 fs), reflecting the decay of the one-exciton coherences that is followed by slow picosecond depolarization due to B800 → B800 migration. Both these processes can be directly viewed by means of the density matrix in the exciton and site representation.

Introduction

Since the discovery of the crystal structure of the peripheral B800−B850 LH2 antenna of purple bacteria *Rhodopseudomonas (Rps.) acidophila*[1] and *Rhodospirillum (Rs.) molischianum*,[2] considerable efforts have been made to understand the physical origins and pathways of the excitation energy transfer within these B800−B850 complexes. The B800−B850 LH2 antenna consists of two rings of bacteriochlorophyll *a* (BChl) molecules: an outer ring with an absorption maximum around 800 nm and an inner ring with an absorption maximum around 850 nm. The energy transfer dynamics includes migration of localized excitations around the BChl 800 outer ring, superimposed with the transfer to the exciton states of the BChl 850 inner ring with subsequent equilibration in the exciton manifold and motion of quasi-steady-state wave packet (delocalized over

4−6 BChl's 850) around the inner ring (see refs 3−5 for review). The possible interplay of intraband B800 → B800 and interband B800 → B850 energy transfer has been the subject of intense studies by hole burning,[6−11] pump−probe,[12−22] and three-pulse photon echo techniques.[23,24]

In one-color pump−probe experiments on *Rhodobacter (Rb.) sphaeroides* at 77 K a monoexponential decay of transient absorption (TA) with a time constant of 1.2 ps was observed in the red side of the 800 nm band.[14] This component was ascribed to B800 → B850 transfer, whereas an additional fast component of 0.45 ps appearing at the blue side of the 800 nm band was taken to reflect the B800 → B800 hopping.

Similar one-color measurements on *Rb. sphaeroides* at 77 K revealed biexponential decays with fast components of 0.33, 0.46, and 0.60 ps and slow components of 1.67, 1.80, and 1.90 ps upon 790, 800, and 810 nm excitation, respectively.[13] The wavelength-dependent slow and fast components were ascribed to interband B800 → B850 and intraband B800 → B800 transfers. This conclusion was further corroborated by anisotropy

* To whom correspondence should be addressed. Fax: +31-20-4447999. E-mail: rienk@nat.vu.nl.
† Moscow State University.
‡ Vrije Universiteit.

measurements that showed fast decay suggesting the pairwise hopping time between BChl's 800 of 0.3 ps.

Two-color pump—probe experiments on *Rb. sphaeroides* at 77 K showed time constants of 1.2 and 0.3 ps that were attributed to B800 → B850 and B800 → B800 transfers, respectively.[20]

Polarized one-color pump—probe kinetics have been measured for the B800 band of the LH2 light-harvesting antenna of *Rs. molischianum* at 77 K.[22] The excitation-wavelength-dependent pump—probe kinetics together with the anisotropy decays (using eight different excitation wavelengths from 788 to 809 nm) allowed a more detailed analysis of the intraband B800 → B800 and interband B800 → B850 transfers. The B800 → B850 transfer time is 1.3 ps on the blue side of the band (788 nm), increasing to 1.9 when tuning to the middle of the band (800 nm) and decreasing to 1.6 ps on the red side (809 nm). The time constant for the fast component increases from 0.3 at 788 nm to 0.8 at 806 mn. The anisotropy decays with approximately the same (about 0.5 ps) time constant, confirming the assignment of the fast component to the intraband B800 → B800 transfer.

Combined two-color pump—probe at 19 K and hole-burning data at 4.2 K indicate a 1.6—1.8 ps B800 → B850 transfer together with an additional fast (0.4 ps) relaxation channel at the blue side of the 800 nm band.[9] The fast component was supposed to have an intra-B800 origin because no corresponding component was observed in the 850 nm photobleaching formation in two-color B800 → B850 measurements.[9] Calculation of the Förster-type rates showed that this fast component could not be ascribed to the B800 → B800 transfer. Alternatively, a coupling of B800 with the upper exciton states of the inner BChl 850 ring (B850*) with subsequent relaxation to the lowest B800 state was suggested.[9] A similar "detour via B850* pigments" scheme, i.e., the fast B800 → B850* → B800 channel, was later suggested by the Redfield theory modeling.[25,26] However, recent high-pressure hole-burning results provided evidence that the B800—B850 mixing is of no importance for explaining the additional fast channel,[11] thus leading back to the conclusion that the direct B800 → B800 transfer is responsible for such a fast relaxation component.[11]

At room-temperature TA measurements gave B800 → B850 transfer times of 0.7—0.8 ps for *Rb. sphaeroides* and *Rps. acidophila*[15—20] and 1.0 ps for *Rs. molischianum*.[21] The experimental transfer times decrease from 1.2 to 0.5 ps upon tuning the excitation wavelength from 790 to 830 nm.[21] Anisotropy decays times (attributed to B800 → B800 transfer) of 0.4—0.8[16] and 0.8—1.2 ps[12,19] were found.

Recently, three-pulse photon echo experiments were performed by Salverda et al.[23] for *Rs. molischianum* and *Rps. acidophila* at room temperature. The intra-B800 transfer times were estimated from the echo peak shift (3PEPS) for these two species as 0.8 and 1.1 ps, respectively. Transient grating (TG) anisotropy decay times (which were ascribed to the B800 → B800 transfer) are 0.9 and 0.7 ps for the same species. The pulse spectrum in this experiment (about 30 nm) is broader than the whole B800 band (in contrast to pump—probe experiments mentioned above, where narrow-band pulses are used for selective excitation and detection within the B800 band). Such a broad-band pump allowed a coherent excitation of vibrational manifold corresponding to the 162 cm⁻¹ mode. Strong oscillations in the echo peak shift for both species reflect long-lived vibrational coherences with damping times of 0.5 and 0.7 (for *Rs. molischianum* and *Rps. acidophila*, respectively) that do not exceed the corresponding hopping times, i.e., 0.8 and 1.1

(3PEPS), and 0.9 and 0.7 (TG anisotropy). Thus, in the model of Salverda et al.[23] vibrational dephasing is not significantly affected by hopping. A similar experiment with 40 nm pulses was performed for *Rps. acidophila* by Agarwal et al.[24] who obtained the 3PEPS data very close to that of Salverda et al.[23] The simulation based on the model of partially correlated disorder gave the B800 → B800 transfer time of 0.5—0.6 fs and the vibrational coherence damping time of 1.5 ps (for the 165 cm⁻¹ mode). In this simulation the time of free vibrational dephasing is larger than the hopping time. It means that the actual decay of oscillatory features displayed by the 3PEPS curves will be significantly shortened due to hopping acts (that were supposed by Agarwal et al.[24] to completely break the memory of the dynamic fluctuations). This actual decay of the 3PEPS oscillations is the same in both experiments, i.e., about 0.5—0.7 ps, so that oscillations have sizable amplitude within about 1 ps.

Theoretical studies of the B800 → B800 and B800 → B850 energy transfers were performed using conventional Förster theory,[9,15,20,24,27] the Förster theory modified to the case of delocalized states of the acceptor[21,28,29] as well as the Redfield theory.[25,26] Comparison of the Förster and Redfield theories with a more general approach[30] showed that in the case of relatively weakly (20 cm⁻¹) coupled pigments with a small (0—100 cm⁻¹) energy gap (which is close to the case of intra-B800 transfers) the Förster theory does not work properly, whereas Redfield gives realistic rates. On the other hand, for a larger energy gap between monomers (200—1000 cm⁻¹), the Förster equation works correctly, whereas Redfield always gives slower rates (see Figure 2b in ref 30). Thus, the interband B800 → B850 transfer probably can be described by the Förster-type theory.[21,28,29] But application of the Förster theory for the intra-B800 dynamics (to explain the wavelength-dependent decay rates) may be connected with serious problems (Wendling, unpublished results). As we will see below, the intra-B800 transfers include dynamics of one-exciton coherences (which strongly influence the anisotropy decay), so that the Förster theory cannot be applied. The Redfield theory seems to be more appropriate to unravel the origins of the intra-B800 and B800 → B850 dynamics.[25,26] More general modified Redfield approach in its present form[30,31] contains the population dynamics only, and thus cannot be used for quantitative modeling.

In this paper we tried to gain more insight into the problem by modeling the isotropic and anisotropic TA kinetics observed using different excitation wavelengths within the 800 nm band of *Rs. molischianum* at 77 K.[22]

In a first attempt we tried to simulate the dynamics in the B800 band with a simple energy transfer model (Wendling, unpublished results). The transfer of excitation energy within the B800 ring was based on the Förster model; the transfer to the B850 ring was not included. The homogeneous absorption spectrum of a B800 pigment was calculated from the Huang—Rhys parameters and the frequencies of the phonon wing and of the vibronic modes given in Figure 3 of ref 20. The width of the zero-phonon-line 46 cm⁻¹ was assumed, which yields a homogeneous line with a full width at half-maximum (fwhm) of *kT*. The mirror image of the homogeneous absorption spectrum was taken as the homogeneous emission spectrum. The overlap integral between donor emission and acceptor absorption was then calculated as a function of their relative positions within the inhomogeneous distribution (Gaussian with fwhm of 110 cm⁻¹). The contribution of each pigment *i* to the anisotropy was calculated by $r_i = (3 \cos^2 \alpha_{ij} - 1)/5$, where α_{ij} is the angle between the transition dipole moments of pigment

i and the originally excited pigment j ($\alpha_{ij} = 360°/|i - j|$). This anisotropy was weighted by the population on pigment i. We found that calculated time-dependent (polarized) spectra do not describe the experimental situation. Changing parameters, as the width of the inhomogeneous distribution or the line shape, could not resolve this problem. We then concluded that using the simple Förster-type hopping model is an oversimplification of the actual situation.

In the modeling presented in this paper we used the Redfield theory in the basis of one- and two-exciton eigenstates of the B800−B850 complex, which enabled us to quantitatively explain the data. The theory includes a proper description of the mixing of the B800 and B850* states (i.e., higher exciton states of the inner BChl 850 ring) in the 800 nm region. The dynamics in this region are described by the density matrix evolution that includes population and coherence transfer (the latter turns out to be essential for a correct interpretation of the fast anisotropy decay). We found that the B800 → B800 population transfer is relatively slow (1−3 ps depending on wavelength), whereas a fast 0.3−0.5 ps anisotropy decay does not reflect any population dynamics but is determined by a decay of the coherences between B800 states. The B800 population dynamics is responsible for the slow (1−3 ps) anisotropy decay component. Energy transfer to B850 is determined by a direct B800 → B850 transfer and a faster (subpicosecond) B800 → B850* → B850 pathway. We also found that the "detour" pathway B850* → B800 is significantly slower than the B850* → B850 relaxation. Below we will see that this energy transfer scheme (with all the details given by the full Redfield tensor) is consistent with the whole set of the 77 K linear and nonlinear (polarized pump−probe) spectroscopy data.

The Model

Hamiltonian System. LH2 antenna of *Rs. molischianum* consists of 8 BChl 800 molecules in the outer ring and 8 BChl 850(α)-BChl 850(β) dimeric subunits forming the inner ring. In our calculation the unperturbed energies of S_0-S_1 transitions in the BChl 800, BChl 850(α), and BChl 850(β) monomers are 12 563, 12 325, and 12 025 cm^{-1}, respectively. These values were used to reproduce the positions of the 800 and 850 nm absorption peaks. The difference between the BChl 850(α) and BChl 850(β) site energies was introduced as suggested in ref 3. The energies of the 1α1β, 1β2α, 1α2α, 1β2β, and 1α2β interactions are +273, +249, −38, −26, and +10 cm^{-1}. The interaction energies were calculated in the point-dipole approximation with the monomeric dipole strength of 55 D^2 and the refractive index of $n^2 = 2$. In this approximation the 1α1β and 1β2α couplings are almost the same (262 and 260 cm^{-1}), in contrast with the point-monopole approach.[5] Increasing the difference between these two values gives a more realistic model. These site energies and couplings were fixed in our modeling. To fit to the experimental line shapes, we have varied the site inhomogeneity values and the system-bath couplings (see below). The ratio of transition dipoles for the S_1-S_2 and S_0-S_1 transitions in the BChl monomer was taken to be 0.5, the S_1-S_2 transition energy is blue shifted by 100 cm^{-1} with respect to the S_0-S_1 transition energy.

The site inhomogeneity of the LH1 antenna was described by uncorrelated perturbations δE to the transition energies of the BChl 800 and BChl 850(α,β) monomers. The inhomogeneous width (fwhm of the Gaussian distribution of δE values) is σ_{800} and σ_{850} for the molecules belonging to the outer and inner ring, respectively.

We are working in the basis of purely exciton eigenstates; i.e., all the phonons and vibrations are treated as a bath with a weak coupling to the system (electronic) coordinates.

Redfield Tensor (System-Bath Coupling). The Redfield tensor used in this paper is defined in Appendix A. The pump−probe response can be expressed through the density matrix equation with the Redfield relaxation operator in the exciton basis as described elsewhere.[32,33] The linear absorption was calculated similarly to the nonlinear absorption (eq 3 in ref 33) but with the first-order density matrix (given by eq A1 in ref 33) in the steady-state (long-pulse) limit. Both linear and nonlinear absorption were calculated using the full (nonsecular) Redfield tensor in the exciton basis (given in general by eq A1 and in more explicit form by eq B2 in ref 33).

The elements of the Redfield relaxation tensor defined by eqs A1 and A2 describe the connection between exciton levels. For example, the population transfer between one-exciton states k and k' is given by the term $\sum_{nmn'm'}c_{nk}c_{mk'}c_{n'k}c_{m'k'}J_{k'k}\langle v_{nm}v_{n'm'}\rangle$, where c_{nk} is the wave function amplitude of the nth molecule participating in the kth exciton state, $J_{k'k}$ is the spectral density of the system-bath coupling, v_{nm} denotes the amplitude of the bath-induced modulation of the one-exciton Hamiltonian (i.e., fluctuations of the site energies and intermolecular couplings for $n = m$ and $n \neq m$, respectively), and brackets indicate an averaging over the bath. We use the simplest model of uncorrelated diagonal disorder with $\langle v_{nm}v_{n'm'}\rangle = v_{800}\delta_{nm}\delta_{n'm'}\delta_{nn'}$ or $v_{850}\delta_{nm}\delta_{n'm'}\delta_{nn'}$ if the nth molecule belongs to the outer or inner ring, respectively. The spectral density was supposed to be the same for the 800 and 850 nm regions, but the corresponding fluctuation amplitudes v_{800} and v_{850} were taken to be different. We use dimensionless v_{800} and v_{850}, whereas the spectral density parameters V_1, V_2, V_0, ω_{c1}, and ω_{c2} (see eq A2) are measured in cm^{-1}. The values of these parameters adjusted from the fit are given in the next section.

In the modeling of the intraband relaxation in the B850-LH2[32] and LH1 antenna[33] the spectral density of the simplest form of $VW^2 \exp(-W)$ was used, where V is coupling strength, $W = \omega_{kk'}/\omega_c$, where ω_c is the characteristic frequency which was varied around 50 cm^{-1}. Notice that in addition to a low-frequency peak ($2\omega_c = 100$ cm^{-1}) the real spectral density contains resonance peaks at higher frequencies.[34,35] But this high-frequency part does not contribute significantly to the intraband relaxation in LH1/LH2. In that case the low-frequency part of the spectral density approximated by some simple shape would be a good model, allowing to quantitatively explain a wavelength-dependent relaxation dynamics.[33]

When the systems with intra- and interband transfers are modeled, like the B800−B850 antenna (with the interband splitting of 500−1000 cm^{-1} depending on which pair of levels is involved), more complicated spectral densities are needed. At least two components should be included, for example, of the form of eq A2. In eq A2 the coupling to high-frequency modes was modeled by one broad structureless peak at $2\omega_c = 740$ cm^{-1}. The total Franck−Condon factor of the high frequency modes of this region can be roughly estimated as $S_2 = V_2\Delta\omega_2/\omega_{c2}^2 \approx 0.05$ for BChls 850 (where $\Delta\omega_2$ is the full width of our high-frequency wing). Similarly, the Huang−Rhys factor for the low-frequency peak is about $S_1 = 0.75$ for BChls 850 at 77 K.

Results

A simultaneous fit of the experimental data including absorption (Figure 1), pump−probe (Figures 2 and 3), and anisotropy kinetics (Figure 4), was obtained for $v_{800} = 0.35$, $v_{850} = 1.4$, $\omega_{c1} = 80$ cm^{-1}, $\omega_{c2} = 370$ cm^{-1}, $V_1 = 60$ cm^{-1}, V_2
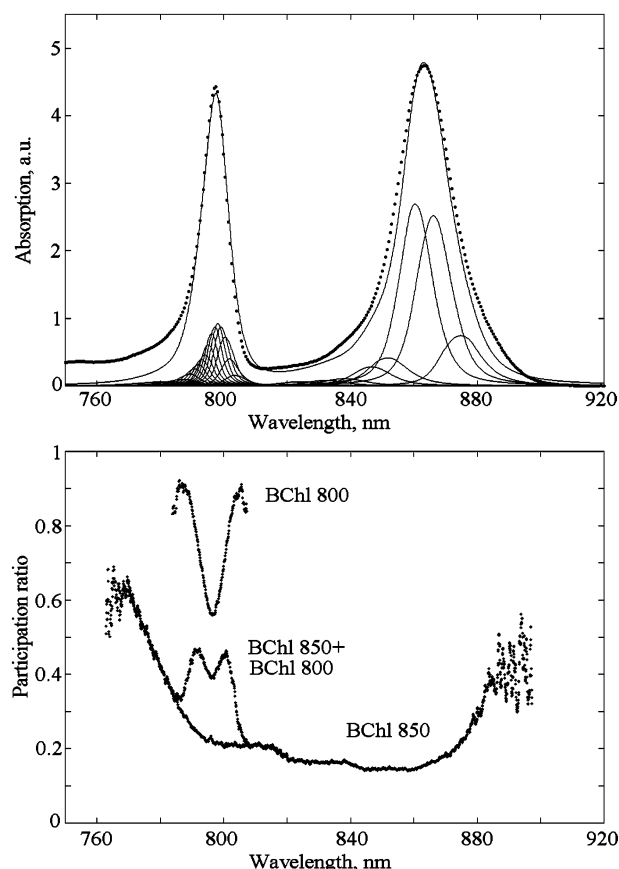
Figure 1. Absorption spectrum of LH2 antenna of *Rs. molischianum* measured at 77 K (points) and calculated using the exciton model (solid line). The line shapes of individual exciton components (solid lines) are obtained by averaging over disorder the homogeneous spectra determined by the Redfield relaxation tensor. The lower frame shows participation ratios calculated for the isolated BChl 850 ring, isolated BChl 800 ring, and the whole LH2 complex (i.e., BChl 850 + BChl 800 rings). Parameters are $\nu_{800} = 0.3$, $\nu_{850} = 1.4$, $\omega_{c1} = 80$ cm^{-1}, $\omega_{c2} = 370$ cm^{-1}, $V_1 = 60$ cm^{-1}, $V_2 = 20$ cm^{-1}, $V_0 = 60$ cm^{-1}, $\sigma_{800} = 120$ cm^{-1}, $\sigma_{850} = 420$ cm^{-1} (see the text for details).

$= 20$ cm^{-1}, $V_0 = 60$ cm^{-1}, $\sigma_{800} = 120$ cm^{-1}, $\sigma_{850} = 420$ cm^{-1}. When the characteristic frequencies ω_{c1} and ω_{c2} are fixed, the coupling strengths V_0, V_1, and V_2 can be determined with high accuracy ($\pm 5-10\%$) because they determine the time scales of the kinetics. The ω_{c1} and ω_{c2} values can be varied within a $\pm 20-30\%$ range, for choices outside this range no good fit can be obtained. The static disorder values σ_{800} and σ_{850} and scaling factors of the dynamic disorder ν_{800} and ν_{850} are very critical to reproduce the broad B850 line and narrow B800 spectrum. This cannot be done without introducing a big difference (about 4 times) between the disorder values for the BChls 800 and 850 (both for the static and dynamic disorder values). Such a big difference is needed if we use a model with uncorrelated disorder, whereas for correlated disorder we will need smaller values of the BChls 850 disorder. Notice that the magnitude of the dynamic disorder for closely spaced pigments can be significantly increased due to charge-transfer interactions, as was suggested for some types of Chl *a* molecules in the PSI complex.[36,37] Charge-transfer states were shown to play an important role for LH1 and the B850-LH2 antenna,[38-40] in contrast to the B800 band. This may be the reason of a big difference in static and dynamic disorder values for BChl's 850 and 800.

Exciton Structure of the Absorption Spectrum. Figure 1 shows the absorption spectrum of the LH2 antenna of *Rs.*
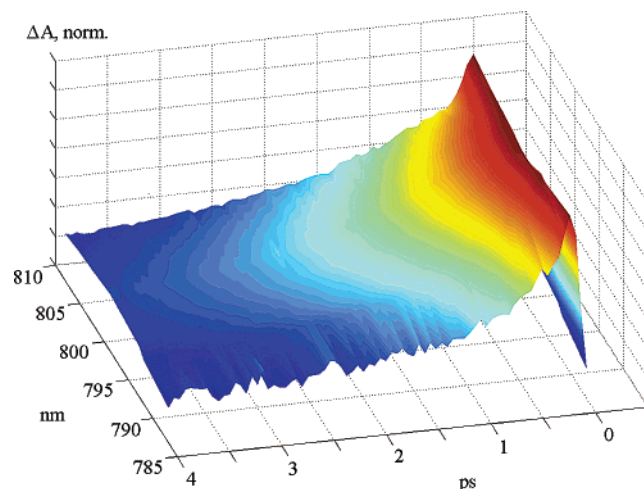

Figure 2. One-color isotropic (magic angle) pump−probe kinetics measured for LH2 antenna of *Rs. molischianum* at 77 K upon excitation in the 800 nm region (Wendling et al., 2003). The difference absorption values are normalized to the maximal bleaching amplitude (reached near zero delay) and inverted. Notice that the decay of the 800 nm band bleaching is accompanied by a formation of the excited-state absorption (ESA) of the 850 nm band (which contributes to the absorption changes near 800 nm). That is why we really normalized absorption changes to the bleaching amplitude minus this quasi-steady-state ESA value. Then, we got decay from the unity to zero for all wavelengths, making it easier to compare the corresponding time scales.
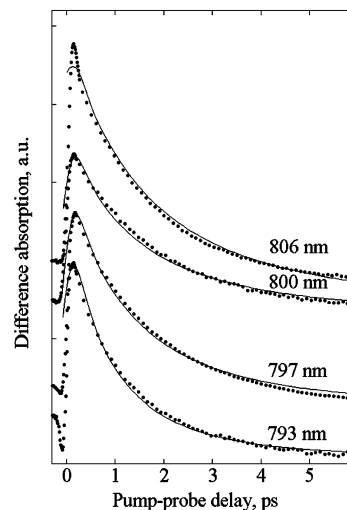

Figure 3. Fitting of the magic angle kinetics for different excitation wavelengths: experiment (points) and calculation (solid lines). Parameters of the model are the same as in Figure 1. Notice that we have calculated the sequential part of the pump−probe response (neglecting the coherence artifact). It means that correct results can be expected only for delays larger that the pulse duration (130 fs).

molischianum measured at 77 K and calculated using the exciton model. The line shapes of individual exciton components were obtained by averaging the homogeneous spectra determined by the Redfield relaxation tensor over disorder. Eight exciton components in the 815−900 nm region correspond to the lowest Davydov component of the inner ring (B850 states). The 770−815 nm region consists of eight exciton states of the outer ring (B800 states) together with the upper Davydov component of the inner ring (B850* states). The lower frame of Figure 1 shows participation ratios calculated for the isolated BChl 850-ring, isolated BChl 800-ring, and the whole LH2 complex (i.e., BChl 850 + BChl 800-rings). The delocalization length is 3−5 BChls for the lowest state, and 6−7 BChls for higher states of the lowest Davydov component. The states of the higher Davydov
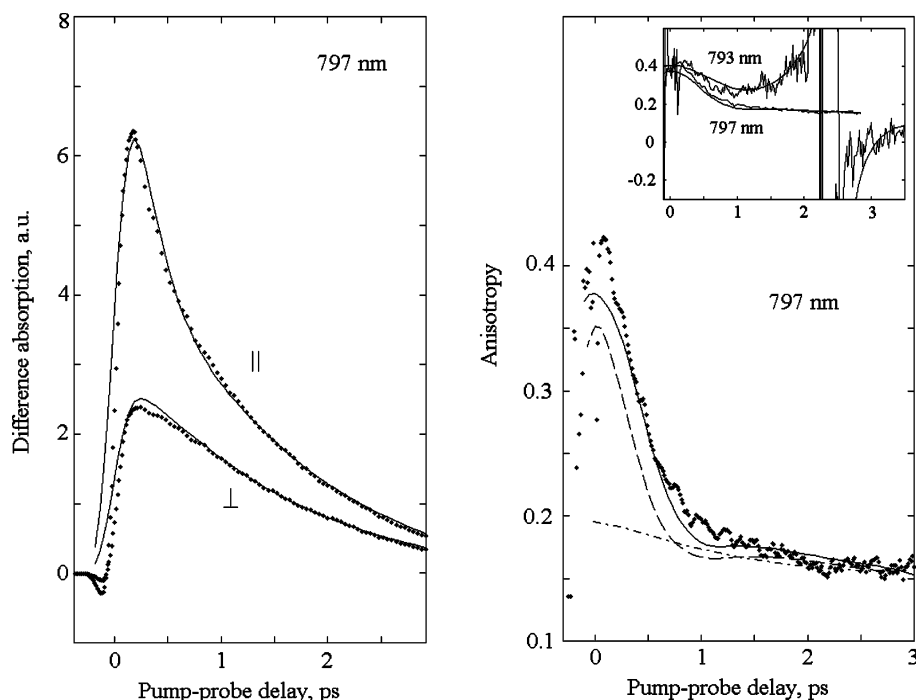
Figure 4. Fitting of the anisotropy kinetics at 797 nm: experiment (points) and calculation (solid lines). Parameters of the model are the same as in Figures 1 and 3. The anisotropy kinetics at 797 nm were calculated using the nonsecular Redfield theory (solid lines), in the secular approximation (dashed curve) and in the noncoherent limit (dash−dotted curve). The calculated parallel and perpendicular transient absorption kinetics at 797 nm are shown in the nonsecular case only (solid lines). Insert shows anisotropy kinetics at 797 and 793 nm, measured (noisy curves) and calculated ones (solid lines). The 793 nm curves (i.e., both measured and calculated) exhibit a singularity point near 2.2−2.5 ps, where transient absorption turns from negative to positive due to bleaching decay accompanied by a formation of the ESA band. The 797 nm curve has the same singularity but the corresponding point is shifted to larger delays due to bigger bleaching values near the center of the 800 nm band.

component of the BChl 850-ring are delocalized to a lesser extent, whereas the exciton states of the isolated BChl 800 ring are almost completely localized (with an inverse participation ratio of 1.1−1.6 BChls). The BChl 850 + BChl 800 participation ratio reflects a noncoherent mixing of the B800 and B850* states in the 780−810 region (the order of B800 and B850* states is different for different realizations of the disorder, so that it is possible to find either a B800 or a B850* state at any fixed wavelength). Such a mixing also results in a smooth distribution of the dipole strength over these 16 mixed states in the 770−815 nm region. The states at the blue and red edges of this band have smaller dipole strength because at the edges the weakly allowed B850* states have higher density (see the dipole strengths and density of states for the B800 and B850* pools shown in Figure 6).

Notice that the absorption spectrum shown in Figure 1 was obtained in the nonsecular approximation (i.e., with taking into account the transfer of the ground-to one-exciton coherences when the first-order density matrix was calculated). Calculation in the secular approximation showed the same positions and intensities of the exciton transitions, but the line shapes of exciton components were found to be slightly different (data not shown). We conclude that the nonsecular terms are not essential for the modeling of linear absorption.

Polarized Pump−Probe Kinetics in the 800 nm Region. Figure 2 shows one-color isotropic (magic angle) pump−probe kinetics measured for LH2 antenna of *Rs. molischianum* at 77 K upon excitation in the 800 nm region.[22] Notice that the decay of the 800 nm band bleaching is accompanied by the formation of excited-state absorption (ESA) of the 850 nm band (that contributes to the absorption changes near 800 nm). To compare the traces, we have normalized the absorption changes (subtracting this quasi-steady-state ESA value) to the difference between maximal bleaching amplitude (reached near zero delay) and
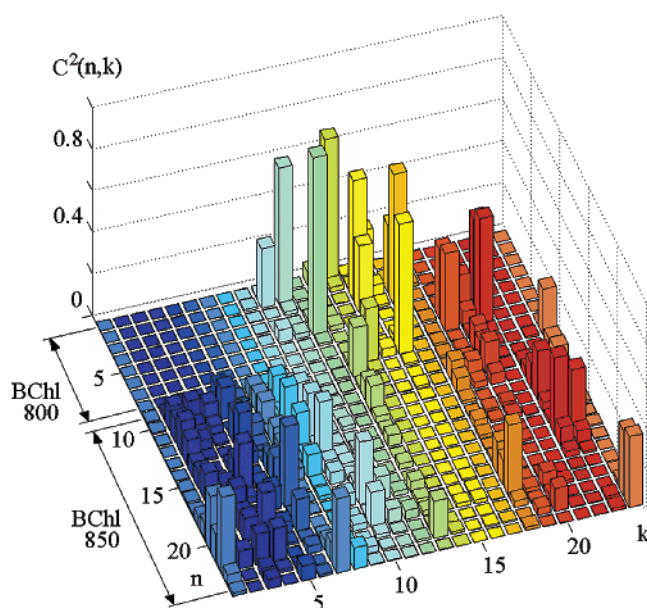

Figure 5. $(c_{nk})^2$ matrix giving a participation of the *n*th molecule in the *k*th exciton state. The c_{nk} values are obtained by diagonalization of the one-exciton Hamiltonian for one realizatoin of the disorder (i.e., the same as shown in Table 1). We number the sites as $n = 1−8$ for BChl's 800 and $n = 9−24$ for BChl's 850 molecules. The exciton states $k = 1−24$ are numbered in increasing order of energy.

steady-state ESA. Then, each trace decays from unity to zero, thus facilitating a comparison between the corresponding time scales. It is seen that the kinetics slow when tuning the excitation to the red side of the 800 nm band, but they become faster in the red-most edge of the band. Such a behavior reflects an interplay of intra- and interband transfer events, so that the fitting of the data must be critical to the choice of free parameters of
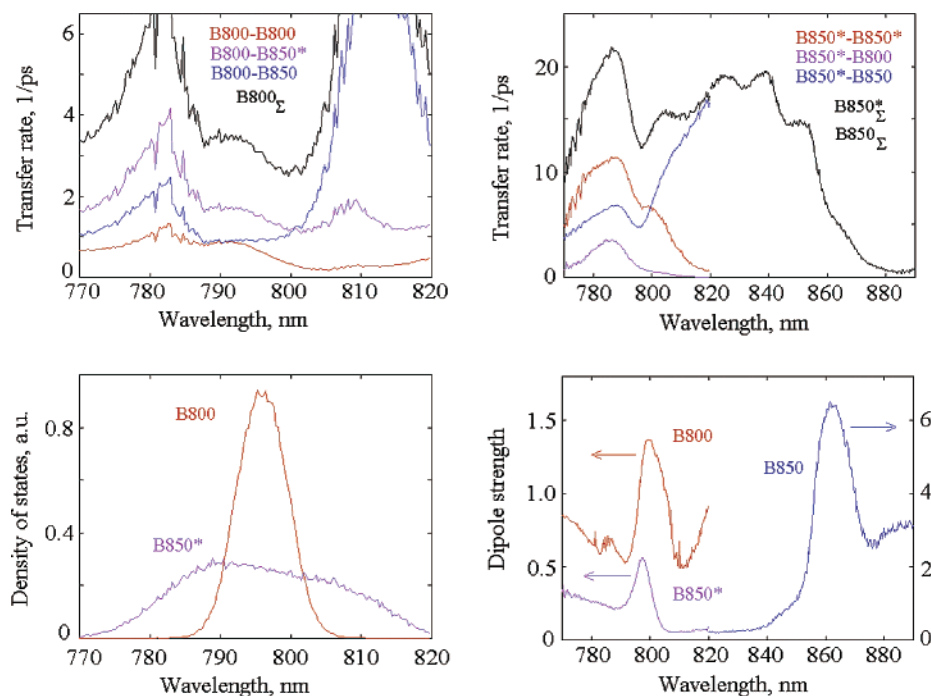
Figure 6. Energy transfer rates in LH2 averaged over disorder with a weight factor reflecting a participation of some group of pigments in the corresponding exciton states (Appendix B). Parameters are adjusted from the simultaneous fit of linear absorption, transient absorption, and anisotropy kinetics (shown in Figures 1, 3, and 4). The exciton states of the outer ring containing BChl 800 molecules and higher and lower Davydov subbands of the inner ring of BChl 850 molecules are denoted as B800, B850*, and B850, respectively. The B850* states are superimposed with the B800 states in the 770−820 nm region. The corresponding densities of states and dipole strengths are shown in the left and right bottom frames. The energy transfers include intraband B800 → B800, B800 → B850*, B850* → B800, and B850* → B850* dynamics, interband B800 → B850 and B850* → B850 dynamics, and the B850 band equilibration. The corresponding rates are shown in the two top frames together with the total decay rates (shown by black) of the B800, B850*, and B850 states. These figures allow us to study the rates and pathways of energy transfer for different excitation conditions.

our model (at least to those that determine the ratio of the transfer rates in the manifold of the B800, B850*, and B850 states). The challenge is to obtain a quantitative fit of the wavelength-dependent kinetics using a realistic parameter set.

An example of the fit is shown in Figure 3. Notice that we have calculated the sequential part of the pump−probe response (neglecting the coherence artifact due to pump−probe overlap). It means that correct results can be expected only for delays larger than the pulse duration (130 fs). The model allowed us to reproduce the experimentally observed slower decay at 797 nm as compared with the 793 nm trace, the even more slow decay at 800 mn, and the faster decay at 806 nm (see the four curves in Figure 3). We found that the nonsecular terms are not very important for the interpretation of the magic angle kinetics: the curves obtained in the secular approximation are almost undistinguishable from those shown in Figure 3 (data not shown).

An additional test of the model is the anisotropy fitting. (We will see below that the major component of the anisotropy decay is connected with the dynamics of the one-exciton coherences, which have only a minor influence on the magic angle kinetics). The fit of the 797 nm anisotropy is shown in Figure 4. The anisotropy kinetics were calculated (i) including all nonsecular terms, (ii) in the secular approximation, and (iii) in the noncoherent limit. The secular approximation implies that the population dynamics is decoupled from the coherences and the coherences exhibit a simple decay (the transfer of the one-exciton coherences in a disordered aggregate with anharmonic level structure can be neglected in a secular approximation[25]). In the noncoherent limit we neglect the contribution from the coherences by taking into account only one-exciton populations given by the diagonal part of the density matrix. The parallel/

perpendicular transient absorption kinetics calculated in the secular and nonsecular cases are hardly distinguishable, so that only the nonsecular case is shown (in the left frame of Figure 4). The anisotropy curves (right frame of Figure 4) are more sensitive to the choice of the physical model, i.e., cases i−iii.

Experimental kinetics of the anisotropy at 797 nm shows a fast decay (from 0.42 to 0.2 with about 0.5 ps time constant), which is followed by a slower picosecond decay (from 0.2 to 0.1 between 1 and 8 ps delays). This behavior is satisfactorily reproduced by our model with taking into account all nonsecular terms. In the secular approximation the calculated anisotropy is less than the measured one, especially during the period of fast decay. This fast component disappears when switching off the coherences, i.e., in the noncoherent limit with taking into account the population dynamics only. In this case the initial anisotropy (of about 0.2 according to our calculation) decays to 0.1 with a few picosecond time constant, thus reproducing the experimental anisotropy dynamics for large delays (i.e., larger than 1 ps). We then conclude that the slow component reflects the one-exciton population dynamics, which corresponds to a hopping between localized B800 states. On the other hand, the fast component is not connected with a migration of the exciton around the BChl 800 ring. This fast component reflects a decay of the one-exciton coherences as well as the coherence transfer. The way population and coherence dynamics influence the anisotropy will be discussed in more detail below.

Notice that 797 nm corresponds to the bleaching maximum of the 800 nm band, where the anisotropy is not strongly affected by ESA contribution from the B850 states. When tuning to the red or blue edge of the 800 nm band, the anisotropy curves $r(t)$ become strongly deformed in the vicinity of the zero-crossing point (where negative TA values turn to positive due to

TABLE 1: Parameters of the Exciton States of LH2 at 77 K Calculated for One Particular Realization of the Disorder

k	λ, nm	D norm.	R_{kkkk}, ps^{-1}	$\Sigma c_{nk}{}^2$, 1 < n < 8	$\Sigma c_{nk}{}^2$, 9 < n < 24
1	870.0	2.89	0.64	0.0002	**0.9998**
2	858.9	4.78	3.86	0.0004	**0.9996**
3	858.0	7.59	8.87	0.0005	**0.9995**
4	849.6	1.25	18.91	0.0007	**0.9993**
5	843.3	0.98	14.94	0.0012	**0.9988**
6	835.9	0.06	22.48	0.0010	**0.9990**
7	827.1	0.23	13.31	0.0018	**0.9982**
8	819.4	0.28	18.68	0.0012	**0.9988**
9	806.6	0.02	**14.46**	0.0189	**0.9811**
10	801.8	0.33	*7.88*	*0.3545*	*0.6455*
11	801.4	1.23	*4.10*	*0.7224*	*0.2776*
12	799.7	1.39	*1.82*	**0.8945**	0.1055
13	798.6	0.01	**15.04**	0.1227	**0.8773**
14	797.5	1.67	*1.22*	**0.9660**	0.0340
15	795.9	0.83	*1.44*	**0.9663**	0.0337
16	795.6	1.26	*2.49*	**0.9284**	0.0716
17	794.4	0.17	*1.72*	**0.9680**	0.0320
18	794.2	0.21	**24.22**	0.0646	**0.9354**
19	792.9	0.71	*7.18*	*0.7281*	*0.2719*
20	792.0	0.91	*18.04*	*0.2949*	*0.7051*
21	791.1	0.13	*2.34*	**0.9556**	0.0444
22	786.5	0.06	21.38	0.0050	**0.9950**
23	783.7	0.26	22.76	0.0012	**0.9988**
24	783.0	0.17	27.43	0.0020	**0.9980**

ᵃ The number of the exciton state k is counted in increasing order of energy, λ is the corresponding wavelength, D is the dipole strength normalized to the monomeric dipole strength, R_{kkkk} is the total decay rate (inverse lifetime of the kth state), and the last two columns show a participation of the BChl 800 (1 < n < 8) and BChl 850 (9 < n < 24) molecules in the kth state. The BChl 800 and BChl 850 participation values are calculated as a sum of the squared wave function amplitude c_{nk} over the outer and inner rings, respectively. Relatively small decay rates for the B800 states are shown by lightface italic; significantly larger decay rates of the B850* states are shown by bold; italic bold shows the decay rates of the mixed states.

formation of the positive ESA wings). Such features appear for wavelengths out of the 795−780 nm region. For illustration (see the insert in Figure 4), we compare the anisotropy kinetics corresponding to 797 and 793 nm. The 793 nm kinetics displays a singularity point near 2.2−2.5 ps where the transient absorption turns from negative to positive. Instead of the 0.42 → 0.2 decay at 797 nm the anisotropy at 793 nm decreases to 0.3 value and then grows to very large values. It is clear that such behavior has nothing to do with any energy transfer or relaxation dynamics. Although we can reproduce this behavior by our model (see the measured and calculated curves at 793 nm in the insert), we believe that the 797 nm data are more relevant and more suitable to unravel the time scales of different relaxation processes together with the corresponding anisotropy amplitudes. Notice that the 797 nm curve also has singularity (the same as for 793 nm), but the corresponding point is shifted to larger time delays without affecting the fast depolarization component (i.e., 0.42 → 0.2 decay with sub-ps time scale).

Figures 1, 3, and 4 demonstrate a simultaneous and quantitative fit of linear absorption and nonlinear (polarized transient absorption) kinetics upon different excitation wavelengths. A variation of the parameters did not lead us to any alternative models. Thus we conclude that our parameter choice adjusted from the fit provided us with a realistic picture within the limits of the physical assumptions (purely exciton basis, Redfield-type relaxation, two-component spectral density, uncorrelated diagonal dynamic disorder). This knowledge of the parameters of the system makes it possible to obtain detailed information about the eigenstates (Table 1 and Figure 5), the relaxation pathways and rates (Figure 6), and excitation wave packet dynamics in the exciton and real space (Figures 7−10).
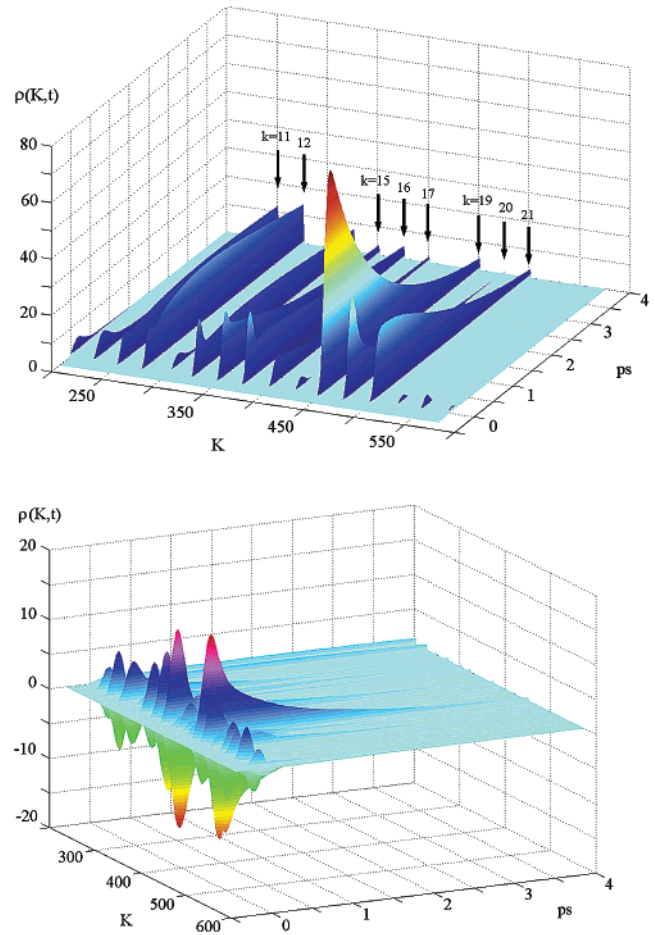

Figure 7. Excitation dynamics in the eigenstates basis upon 788 nm excitation. To exclude a mixing due to static disorder, we use one realization, i.e., the same as was used in Table 1 and Figure 5. The time dependent density matrix $\rho(K,t)$, where $K = k + (k' − 1)N$ is the number of the one-exciton state in a Liouville space $\{k,k'\}$ is shown. Only the 800 nm region states corresponding to $k' = 9−24$ are shown The top frame shows only one-exciton populations (corresponding to $k = k'$, as indicated by arrows), bottom frame shows imaginary part of the coherences (corresponding to $k \neq k'$).

Parameters of the Exciton States. We start with a more detailed study of the exciton states structure. It is convenient to begin with just one realization of the disorder, when the B800 and B850* states are not mixed. Parameters of the exciton states for one particular realization are given in Table 1 and Figure 5. (The energy transfer dynamics for the same realization will be discussed below—see Figures 7−10.)

The eight lowest states (819−870 nm) correspond to the lowest Davydov component of the inner ring (in Figure 1 we have seen the shape of this lowest Davydov band averaged over disorder). These states (we denote them as B850) are determined by excitonic interaction of the BChl850 molecules (with the participation values for the $k = 1−8$ states of >0.998, as shown by bold in Table 1). The largest part of the dipole strength of the inner ring is concentrated in two levels (second and third ones), whereas the lowest level and higher ones borrow some dipole strength from these two. The lowest state is long-lived (1.4 ps for the realization shown in Table 1), and the next two intense levels have shorter lifetimes (260 and 115 fs) due to relaxation to the lowest state, whereas higher states are characterized by ultrashort 40−70 fs lifetimes due to downhill relaxation to the manifold of lower states. Notice that these lifetimes determine the relaxation-induced part of the homo-
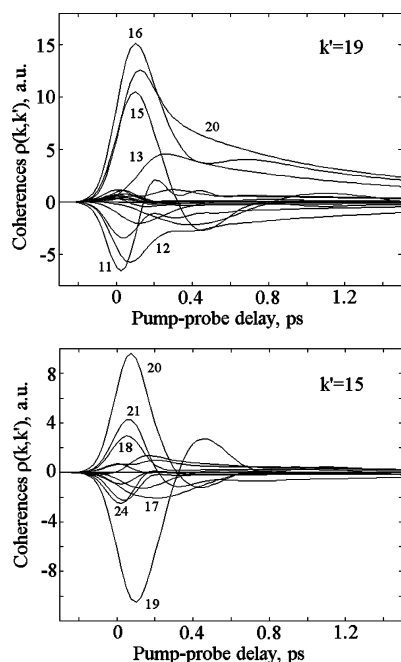
Figure 8. Coherence decay $\rho(K,t)$ as in Figure 7, but shown separately for $K = 436-455$ and $K = 348-360$. These two regions correspond to $k' = 19$ and $k' = 15$ (and k running values from 4 to 23 and 12 to 24, respectively). The curves with the biggest coherence amplitude are labeled by numbers corresponding to the k values.

geneous broadening, whereas another part is given by pure dephasing.

The 791−806 nm region consists of noncoherently mixed states with predominant participation of either BChl 800 or BChl 850 molecules (the corresponding participation values are typically more than 0.87 as shown by bold in Table 1). These states correspond to the exciton states of the BChl 800 ring and exciton states from the higher Davydov component of the BChl 850 ring (it is convenient to denote these states as B800

and B850*, respectively). Depending on the particular realization of the disorder we can find different orderings of these states (with arbitrary order of energy). Some of the states in this region may have comparable participation of BChl 800 and BChl 850 molecules (see, for example, participation values of the 10th and 11th levels and of the 19th and 20th states in Table 1, marked by bold italic). The B800 states have relatively small decay rates (1.2−2.5 ps^{-1}, lightface italic in Table 1) and dipole strength around unity. The B850* states have significantly larger decay rates (14−24 ps^{-1}, bold in Table 1) and small dipole strengths (no more than 0.2). The mixed states are characterized by dipole strengths around unity due to presence of the BChl's 800 contribution, and by increased decay rates value due to mixture with the BChl's 850.

The 783−787 nm region is determined by purely B850* states with very low dipole strengths (0.06−0.26) and very fast decays (21−28 ps^{-1}). Notice that after averaging over disorder there is no distinct boundary between the region of mixed B800 and B850* states and the region of higher B850* states, but these higher B850* states can be seen as a small blue wing (760−785 nm) of the 800 nm absorption band (see Figure 1).

The $(c_{nk})^2$ matrix giving the participation of the nth molecule in the kth exciton state is shown in Figure 5. Here c_{nk} is the eigenfunction amplitude obtained by diagonalization of the one-exciton Hamiltonian. The states from $k = 1$ to 9 are delocalized (nonuniformly) over BChl's 850. The $k = 10$ and 11 states are localized at $n = 2$ molecule of the BChl 800 ring with some coherent admixture of the BChl's 850. The $k = 13$ and 18 states belong to the 800 nm region, but they are delocalized over BChl's 850. The $k = 12, 14, 15, 16$, and 17 states are localized at BChl 800 molecules $n = 5, 1(8), 3(4), 8(1)$, and $4(3)$, where numbers in parentheses indicate some coherent admixture of neighboring BChl 800 molecule due to partial delocalization within the 3−4 and 1−8 dimers (molecules $n = 1$ and 8 are neighbors in the ring of 8 BChl's 800). The $k = 19$ and 21 states correspond to a uniform delocalization over the $n = 6-7$ dimer with a small admixture of the BChl's 850 ($k = 19$ state).
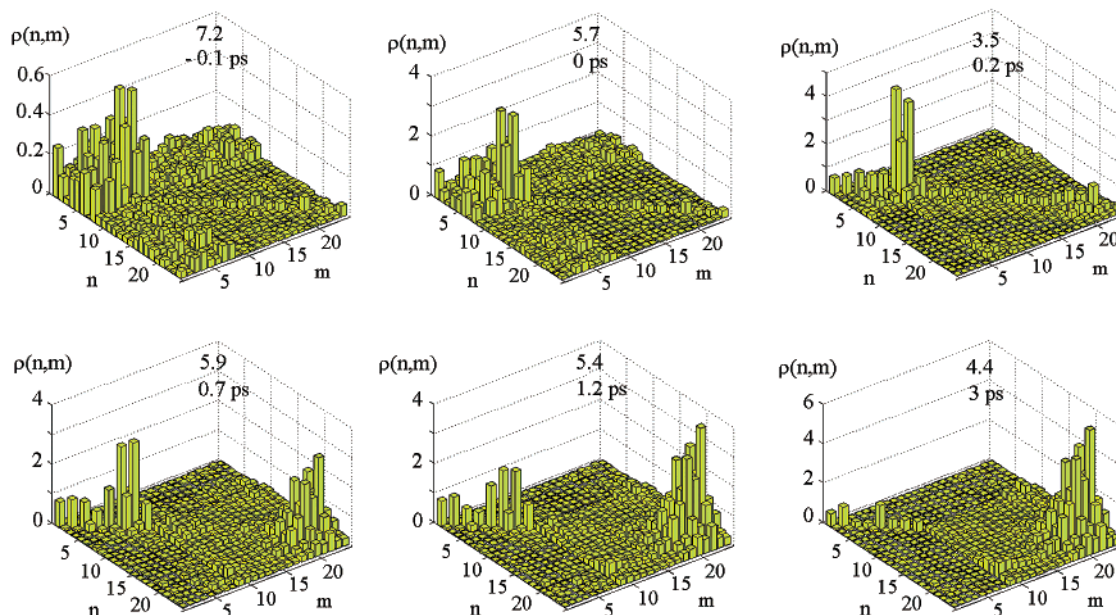

Figure 9. Dynamics of the one-exciton density matrix in the site representation upon blue-side excitation (788 nm) of the B800 band for one particular realization of the disorder (the same as in Table 1 and Figures 5 and 7). Time delays calculated from the maximum of the excitation pulse (130 fs duration) are −0.1, +0, +0.2, +0.7, +1.2, and +3 ps. The absolute values of the density matrix elements $\rho(n,m)$ are presented in arbitrary units that are the same for all panels (note the different scale for the first panel corresponding to a negative delay). We number the sites as $n = 1-8$ for BChl's 800 and $n = 9-24$ for BChl's 850 molecules ($n = 1, m = 1$ corresponds to the left corner of the panels). The degree of delocalization (shown together with time delay) is calculated as the inverse participation ratio N_ρ of the density matrix (Meier et al., 1997).
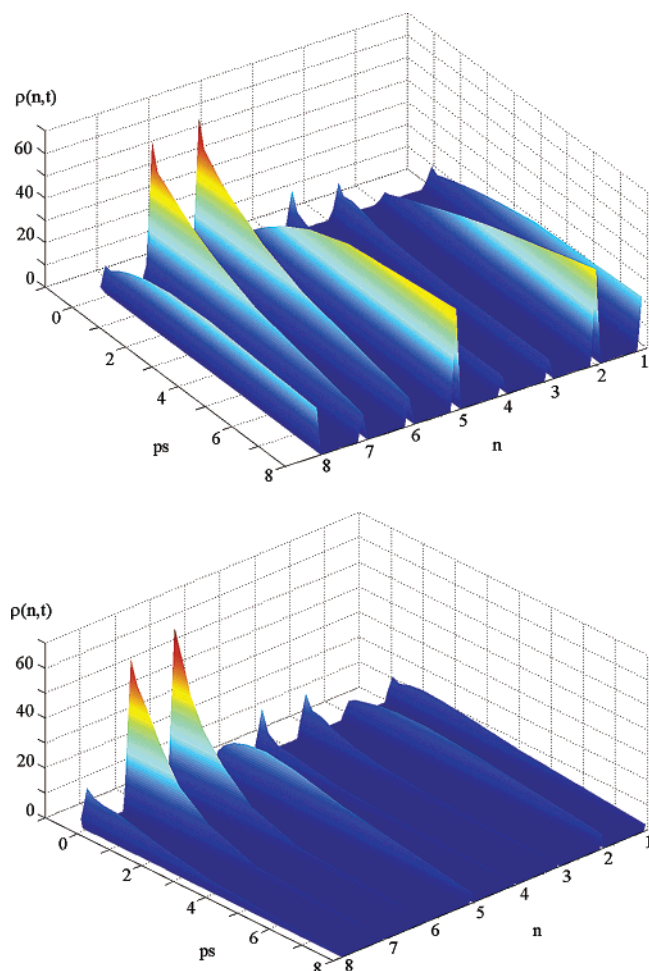
Figure 10. Population dynamics $\rho(n,t)$ of the nth BChl 800 molecule in the case of an isolated BChl 800 ring (top frame) and for the whole LH2 complex, i.e., with the presence of the interband transfer (bottom frame). The data are obtained for one particular realization of the disorder (the same as in Figure 9).

The $k = 20$ state is mixed with comparable participation of the BChl's 800 and BChl's 850.

Notice that other realizations of the disorder typically give a very similar picture, but with a different ordering of the states in different realizations. It is clear that the identity of the states (i.e., difference between B800 and B850* states) will be lost after averaging over disorder. Instead of the data shown in Table 1 (that highlights the different nature of the B800 and B850* states), we will get a smooth distribution of some average dipole strengths and decay rates. It is much more informative to average the dipole strengths and relaxation rates with a weighting factor reflecting the participation of some group of pigments in the corresponding exciton states (see Appendix B).

Energy Transfer between B800, B850*, and B850 Pools. Energy transfer rates averaged over disorder are shown in Figure 6. The data are calculated with the parameters adjusted from the simultaneous fit of linear absorption, transient absorption, and anisotropy kinetics (shown in Figures 1, 3, and 4).

The exciton model gives us three groups of eigenstates: exciton states of the outer ring containing BChl 800 molecules and higher and lower Davydov subbands of the inner ring of BChl 850 molecules. As discussed above, we denote them by B800, B850*, and B850, respectively. The boundary between B850 and B850* is smoothed due to disorder and corresponds to the region 815−820 nm. Equations B4, B5, and B6 allow us to analyze separately the rates of transfer between these three groups of states, as well as transfers within each group (Figure 6, two top frames). Similarly, we can obtain the density of states (eq B2) and dipole strengths (eq B3) for these three groups as shown in Figure 6, left and right bottom frames, respectively.

The dipole strength distribution is connected with the degree of delocalization of the states. In the localized limit the dipole strength shows a uniform distribution over the exciton states, whereas in the delocalized case the dipole strength can be concentrated in a few exciton levels. Thus, the B850 states lying below 820 nm are to some degree delocalized over the inner ring. As a result, the second and third states (850−870 nm) carry the largest part of the total dipole strength of the inner ring. The dipole strength of these states is about 5−6 (in units of the monomeric dipole strength). The dipole strength of the lowest state (870−890 nm) is 2.5−3.5 (notice that this value is in agreement with the measured superradiance[41]). The B800 dipole strength distribution shows the same dependence as the inverse participation ratio (see Figure 1). The enhancement of the dipole strength does not exceed 1.35, reflecting the localized character of the B800 states. The B850* states (almost forbidden in the homogeneous limit) are weakly allowed due to borrowing of some part of dipole strength from the B800 states. The ratio of the densities of states and dipole strengths indicates that upon excitation in the middle of the band (i.e., within 793−800 nm) the B850* states can be directly excited with a 15−25% probability. This probability increases significantly upon blue-side or red-side excitation.

The possible energy transfers include intraband B800 → B800, B800 → B850*, B850* → B800, and B850* → B850* dynamics, interband B800 → B850 and B850* → B850 transfers, and intraband B850 → B850 equilibration. The corresponding rates are shown in the two top frames of Figure 6 together with the total decay rates (inverse lifetimes) of the B800, B850*, and B850 states. These data allow us to study the pathways and time scales of energy transfer upon different excitation conditions.

We start with the 790−800 nm region where the B800 states are predominantly excited. The subsequent dynamics includes migration around the outer ring with 1−3 ps time constant (the B800 → B800 transfer rate decreases from 1 to 0.3 ps^{-1} when tuning from 790 to 800 nm), 1 ps transfer to the inner ring (B800 → B850 transfer), and 500−800 fs transfer to higher states of the inner ring (B800 → B850* transfer). The dynamics of the B850* states is characterized by 100−200 fs downhill B850* → B850* relaxation, 60−200 fs relaxation to the B850 states (higher rates correspond to the red shifted B850* states), and much slower back B850* → B800 transfer. The transfer to the inner ring from B800 and B850* states is followed by an equilibration in the B850 manifold. The relaxation from higher B850 states occurs with a time scale of 50−100 fs. Notice that the B800 → B800 and B800 → B850* transfers are faster for the blue side (within the 790−800 nm region). Such a situation is typical for a manifold of states with predominant downhill transfer. This is the reason for the experimentally observed slowing down of the TA kinetics when tuning from 793 to 800 nm.

At each side of the 790−800 nm region the kinetics are faster because B800 states exhibit faster transfer to B850* at the blue side (<790 nm) and faster transfer to B850 at the red side (>800 nm). As a result, the wavelength dependence of the total decay rate of the B800 states (i.e., the sum of all relaxation rates that is shown in Figure 6, left top frame) shows a decrease from 790 to 800 nm and a sharp increase out of this region. This dependence looks very similar to the wavelength-dependent

decay of the measured kinetics (see Figures 2 and 3). The fast component to the blue of the 790−800 nm region is to some extent also determined by the increase of the relative contribution of directly excited B850* states.

From Figure 6 we may conclude that there are two pathways of energy transfer from the outer to inner ring: the direct transfer from BChls 800 to the lower B850 band and transfer through higher B850* band. Following transfer to B850* we get B850* → B850 relaxation that is much faster than the back B850* → B800 transfer, so that the relative contribution of the B800 → B850* → B850 and B800 → B850 pathways is determined by the rates of the B800 → B850* and B800 → B850 transfers. In the middle of the band (i.e., near 798 nm) these rates are almost equal, at the blue-side (near 790 nm) the transfer to B850* is faster, whereas at the red side (>800 nm) the direct transfer to B850 is faster. It means that the relative contribution of the B800 → B850* → B850 pathway is equal (or at least comparable) to the contribution of the direct B800 → B850 transfer. Both these contributions together with the intraband B800 → B800 transfer will determine the kinetics of the B800 decay. The impact of the B800 → B800 transfer can be studied by anisotropy kinetics (but the latter is also strongly influenced by coherences between one-exciton states of the B800 band).

It should be noticed that Figure 6 shows only transfer rates corresponding to population transfer. Generally, the one-exciton dynamics includes also coherences between exciton states. As was discussed above the coherence dynamics determines the fast component of the anisotropy decay, whereas the slow picosecond depolarization is determined by the B800 → B800 population transfer. Such a two-component decay of anisotropy was theoretically studied for a dimer,[42] where the fast depolarization due to coherence decay is followed by a slower component reflecting the hopping (for more details see Discussion). In this respect it is interesting to compare the time scale of the coherence decay in the BChl 800 ring (obtained in our modeling) with the coherence decay kinetics measured for a dimeric B820 subunit[43] and bacterial reaction center (RC).[44]

The electronic coherence within the special pair P decays with a 35 fs time constant, whereas the coherence between H and B transitions in RC decays with a 96 fs time constant at room temperature.[44] Similar dynamics of the electronic coherence was observed for the B820 dimer.[43] In our model the calculated lifetimes of the coherences between the one-exciton B800 states (i.e., the states of the outer ring) at 77 K are 100−150 fs depending on state and realization of the disorder. This is significantly less than the lifetimes of the B800 states (about 300 fs, see Figure 6 left top) due to a contribution of pure dephasing to the coherence decay. This pure dephasing contribution is not sensitive to alterations of the structure (and energy transfer rates) of the complex (with an accuracy proportional to the exchange narrowing, i.e., a reduction of the pure dephasing in proportion to the inverse participation ratio, see ref 33). For example, similar coherence lifetimes (130−180 fs) have been calculated within the limits of our model for an isolated BChl800 ring, where the population lifetimes are 1−3 ps. Another interesting phenomenon appearing in our modeling is the difference between the coherence lifetimes (100−150 fs) and the time scale of the total coherence decay (about 300−500 fs as revealed by the anisotropy decay). The total time is significantly larger due to (i) coherence transfer in the manifold of one-exciton B800 states of the outer ring, (ii) nonsecular terms connecting populations and coherences dynamics, and (iii) continuous generation of coherences during the 130 fs pump pulse.

Excitation Dynamics in the Exciton Basis. Now we visualize the excitation dynamics using the density matrix. To exclude the mixing of states due to static disorder, we return to one realization; i.e., we use the same realization as was used in Table 1 and Figure 5. Figure 7 shows the time dependent density matrix $\rho(K,t)$, where $K = k + (k' - 1)N$ is the number of the one-exciton state in Liouville space $\{k,k'\}$. The one-exciton populations and coherences (corresponding to $k = k'$ and $k \neq k'$, respectively) are shown for the 800 nm region ($k' = 9-24$) upon 788 nm excitation. Figure 8 shows the coherence decay $\rho(K,t)$ for $K = 436-455$ and $K = 348-360$. These two regions correspond to $k' = 19$ and $k' = 15$ (and k running values from 4 to 23 and 12 to 24, respectively).

The 788 nm excitation results in population of the $k = 19-21$ states with predominant excitation of the $k = 19$ state corresponding to the lowest state of the $n = 6-7$ dimer (see top frame of Figure 7). The $k = 20$ state belongs to B850* and shows a fast decay. The $k = 14-17$ states belong to B800 and have significant dipole strength for this realization (see Table 1), but they are only weakly excited by the red wing of the pump pulse spectrum. The B800 → B800 downhill transfer results in population of the $k = 11$ and 12 states. The B800 → B850* transfer to the $k = 9, 10, 13$, and 18 states is compensated by the fast B850* → B850 relaxation, so that the populations of these B850* states are negligible.

The coherences between one-exciton states exist for 0.5−1 ps (bottom frame of Figure 7). The coherences between the states including highly populated ones ($k' = 19$, top frame of Figure 8) show a relatively long-lived tail due to nonsecular population-to-coherence transfer, whereas coherences including other states ($k' = 15$, bottom frame of Figure 8) increase during the action of the pump with subsequent fast oscillatory decay. Notice a significant coherence between the B800 and B850* states (between $k' = 19$ and $k = 13$ and 20 (top frame) and between $k' = 15$ and $k = 18, 20$, and 24 (bottom frame)). Although the B850* population shows fast decay, the B800−B850* coherence can exist much longer due to nonsecular transfer from populations. This is the case for the coherence between $k' = 19$ and $k = 13$ and 20, which shows nonoscillatory decay (because the fast B850* relaxation break the phase of oscillations). On the other hand the B800−B800 coherences (between $k' = 19$ and $k = 11, 12, 15$, and 16 (top frame) and between $k' = 15$ and $k = 17, 19$, and 21 (bottom frame)) are oscillating reflecting the fact of slower dynamics of the B800 populations.

Exciton Dynamics in the Site Representation. Figure 9 shows the dynamics of the one-exciton density matrix in the site representation upon blue-side excitation (788 nm) for the same realization of the disorder as in Table 1 and in Figures 5 and 7. Time delays calculated from the maximum of the excitation pulse (130 fs duration) are −0.1, 0, +0.2, +0.7, +1.2, and +3 ps. The density matrix elements $\rho(n,m)$ are presented in arbitrary units that are the same for all panels (note the different scale for the first panel corresponding to a negative delay). We number the sites as $n = 1-8$ for BChl's 800 and $n = 9-24$ for BChl's 850 molecules. The degree of delocalization (shown together with time delay) is calculated as the inverse participation ratio N_ρ of the density matrix.[45]

At the very first moment, in the leading edge of the pulse, we observe an almost uniform, coherent excitation of the whole BChl 800 ring (see the panel for −0.1 ps, which displays more or less uniform excitation of populations $\rho(n,n)$ and coherences $\rho(n,m)$ for $n,m = 1-8$). There is also some population of the BChl's 850 due to direct excitation of the B850* states and

some coherence between BChl's 800 and 850 due to coherent superposition of the B800 and B850* states. Subsequently, the polarization approaches a stationary limit, and the pulse starts to feel the overlap between its spectrum and the absorption spectrum. From this point (see the panels for delays 0 and 0.2 ps) only those exciton components grow in amplitude that are in resonance with the pump. The switch from uniform to selective excitation is accompanied by a decrease in the delocalization degree from 7.2 to 3.5 between -0.1 and $+0.2$ ps delay. In our example the pump is in resonance with the $k = 19-21$ exciton states. The $k = 21$ state is only weakly allowed, the $k = 20$ state has a large dipole strength, but its lifetime is shorter than the pump pulse. As a result, the initial population (reached immediately after the pump, i.e., at 0.2 ps) is maximal for the $k = 19$ state (see Figure 7), which is delocalized over the $n = 6-7$ dimer (as we have seen in Figure 5). The corresponding density matrix in the site representation shows pronounced populations $\rho(6,6)$, $\rho(7,7)$ and coherences $\rho(6,7)$, $\rho(7,6)$ together with weaker population and coherences between other states (see the 0.2 ps panel).

From 0.2 to 1.2 ps, when the antenna is no longer interacting with the pump, the coherences between BChl's 800 decay rapidly, leading to the formation of an almost localized (diagonal) density matrix in the $n,m = 1-8$ region. This coherence decay is accompanied by a decrease of the anisotropy with the same time constant (see fast anisotropy decay between 0 and 1 ps in Figure 4). It is important to note that there is no significant migration around the outer BChl800 ring during this period in contrast to what has been suggested in earlier studies (see Introduction).

The period from 1.2 to 3 ps is characterized by significant changes in the population distribution between the $n = 1-8$ sites. We have seen that picosecond relaxation in the B800 manifold results in depopulation of the initially excited $k = 19-21$ states (delocalized over $n = 6-7$ molecules) with population of the lowest $k = 11$ and 12 states localized at $n = 2$ and 5 molecules, respectively. This slow (picosecond) migration around the BChl800 ring from the $n = 6$ and 7 to $n = 2$ and 5 sites is illustrated by the 1.2 and 3 ps panels. Such a migration within BChl's 800 is accompanied by a transfer from the outer to inner ring that reduces the total population of the B800 states and increases the B850 population. The formation of the B850 wave packet (with delocalization degree of $4-6$) determines the relatively high delocalization value for the 0.7, 1.2, and 3 ps time frames. Notice that the isolated outer ring will give N_ρ of about $1.2-1.5$ for these delays.

From Figure 9 it is difficult to separate the contributions of the intraband B800 → B800 migration from the interband B800 → B850 transfer. To observe it in more detail, we calculated the density matrix of the BChl800 molecules for the case of an isolated BChl800 ring (Figure 10, top frame) and for the whole LH2 complex, i.e., with the presence of the interband transfer (Figure 10, bottom frame). The data are obtained for the same realization of the disorder and the same excitation conditions as used in Figures 7 and 9. We have shown the time dependent populations of BChl's 800 ($n = 1-8$). In both cases there is a migration from the $n = 6$ and 7 to $n = 2$ and 5 molecules. The corresponding time constant of a few picoseconds can be seen from the isolated case. For the whole antenna one can see the same migration but superimposed with a faster transfer to the inner ring. This result illustrates the fact that the B800 → B800 migration is slower than the interband transfer (including the B800 → B850 and B800 → B850* → B850 channels) in agreement with the data shown in Figure 6.

Discussion

In this paper we tried to understand a problem that has been a subject of intense study and controversial debate over the past 20 years:[46] the competition between energy transfer within the B800 ring of weakly coupled pigments and transfer from this ring to the strongly coupled B850 ring (see Introduction). One of the most intriguing features is the fast 300−500 fs component observed experimentally both for magic angle kinetics and for anisotropy decay, which so far has remained unexplained. Because anisotropy dynamics reflects an intra-B800 transfer, this component was ascribed to some kind of intraband processes, i.e., fast B800 → B800 migration or/and the fast "detour" B800 → B850* → B800. According to our modeling both these processes are slow. We explain the fast isotropic component by B800 → B850* → B850 relaxation (giving the B800 decay time of 500 fs at the blue side of the 800 nm band, or 300 fs in combination with downhill B800 → B800 relaxation—see Figure 6). However, such an interband relaxation cannot account for the fast anisotropy component. The latter is connected with the decay of one-exciton coherences (300−500 fs), which in turn does not contribute significantly to the isotropic kinetics. Thus, we have two different physical origins giving similar (fast) decay times in isotropic and anisotropic kinetics. Moreover, these two are different from the intraband B800 → B800 relaxation, which was believed to be the origin of the fast decay.[9,11−22,25,26] This intraband relaxation indeed is present both in anisotropy and in magic angle kinetics, but as a slow component. Also its contribution to the anisotropy magnitude is no more than 0.2. Even if we artificially increase the rate of the B800 → B800 transfer, it will remain impossible to explain the measured value of the initial anisotropy of 0.4.

Population and Coherence Part of the Anisotropy Decay. The anisotropy of the nonlinear spectral response (time-resolved fluorescence or pump−probe) allows a visualization of intermolecular energy transfer. For example, migration between chromophores with parallel transition dipoles conserves the initial anisotropy value of 0.4, but for perpendicular dipoles anisotropy drops to 0.1. In the case of strongly coupled chromophores the situation is more difficult. Coherent excitation of two exciton states of a dimer allows us to reach anisotropy values up to 0.7. After decay of the coherence between the two states this value decreases to 0.4 with a subsequent decay to 0.1 due to population relaxation. A theory of the spontaneous or stimulated emission (SE) anisotropy in a dimer was developed by Knox and Gülen,[42] Wynne and Hochstrasser,[47] and Matro and Cina.[48] A similar calculation for more complicated systems such as LH1 and the B850-LH2 antenna was done by Kumble and Hochstrasser[49] and Kühn et al.[50] It was concluded that the initial ultrafast (sub 100 fs) depolarization in fluorescence up-conversion[51,52] and pump−probe measurements[53−56] is connected with the decay of the one-exciton coherences.[49] The high anisotropy due to coherence between initially excited eigenstates is always present, i.e., in the case of both delocalized and localized eigenstates.[49] Although the theory predicts an initial value of 0.7, the experimental values can be significantly less, lying between 0.7 and the incoherent limit of 0.4,[53−55,57] or even lower than 0.4.[51,52] It depends on excitation conditions (pulse duration and wavelength) and the experimental scheme (for example, pump−probe anisotropy determined by superposition of the SE, photobleaching PB, and ESA contributions can be different from the pure SE anisotropy in the fluorescence measurements). Also, coupling to vibrations can have a dramatic effect on anisotropy. Supposing a coupling of the ground states of the pigments to different local vibrations[48] it is possible to

obtain contributions giving 0.4 even in the presence of coherent excitation. These contributions can outweigh the coherent contributions if phonon/vibrational subbands are involved in the measurement.

In the B800 anisotropy measurements[22] the 8 nm (fwhm) pulses were broad enough to create a coherence between strongly overlapping exciton components in the 800 nm region (see Figure 1). Simple analytical calculation (Appendix C) shows that the SE anisotropy for a pair of states with perpendicular dipoles decays from 0.7 to 0.4 due to decay of the coherence between these two states, and then further decays to 0.1 due to population equilibration. The photobleaching component (PB) is characterized by time-independent anisotropy of 0.1. Then the SE + PB signal (far from two-exciton resonances) gives the decay from 0.3 to 0.2 (during the period of coherence decay) and further to 0.1 (during population equilibration period). The whole SE + PB + ESA anisotropy shows the initial (coherent) values of about 0.3−0.35, the incoherent values of 0.15−0.25, and thermalized values close to 0.1. (This estimation is valid for the wavelength near the centrum of the 800 nm band, whereas tuning to the blue or red edge will increase the total anisotropy values for 0−2 ps delays due to singularities near the zero-crossing point.) This example demonstrates that the pump−probe anisotropy values can be significantly less than the SE anisotropy ones. This rough estimation gives the initial value close to the exact numerical result of 0.38 (see Figure 4) and predicts correctly the anisotropy decay from about 0.2 to 0.1 during the population period. Thus, the experimentally observed 0.42 value seems to be an evidence for a coherent superposition of the states.

In this paper we did not model the B850 anisotropy. According to preliminary calculation the B850 anisotropy shows the same dynamics as the B800 anisotropy (shown in Figure 4), i.e., two-component decay with the same amplitudes of the fast and slow components. The difference is that the corresponding times for B850 are about 4−5 times faster than in B800; i.e., the fast component (due to coherences decay) is 60−100 fs and slow component (due to population dynamics) corresponds to 200−600 fs (data not shown). These time scales and amplitudes are in agreement with the experiment.[52−55] Notice that the experimental B850 anisotropy showed a fast decay from 0.37 to 0.4 to 0.15−0.2 with further slow decay to 0.1[54] similarly to the measured B800 anisotropy near 800 nm.[13,22] So, we believe that physics of the anisotropy dynamics is basically the same for B850 and B800, although the delocalization degrees and relaxation rates for these two bands are very different.

Nonsecular Theory vs Secular Approximation. Figure 4 shows the anisotropy kinetics obtained with the full Redfield tensor (including all nonsecular terms) and using the secular approximation. The secular approximation gives faster anisotropy decay, giving rise to lower anisotropy values for short delays (between 0 and 2 ps). The nonsecular theory predicts more long-lived coherences and higher anisotropy values for these delays due to mixing between populations and coherences (see Figure 8 and discussion in the section "Excitation Dynamics in the Exciton Basis"). For larger delays the difference between these two limits vanishes. Very similar results were recently obtained for the fluorescence anisotropy decay in the B850 antenna.[50] Thus, the difference between anisotropy decays calculated for B850 with the full Redfield tensor and in the secular approximation (Figure 6A in ref 50) is essentially the same as in our study (Figure 4, right frame). Both studies gave almost the same ratio between the secular and nonsecular

anisotropy values, but the absolute values of the initial anisotropy and the time scales of its decay are different. As discussed above, the initial anisotropy value for fluorescence is higher (about 0.7 instead of 0.3−0.4 for transient absorption) and also the time scale of the decay is 4−5 times faster for B850 than for B800 antenna (the period of 0−2 ps delays for B800 corresponds to 0−400 fs delays for B850). We also found a different secular and nonsecular initial anisotropies in contrast with ref 50. Notice that in our modeling we have taken into account the relaxation dynamics during the pump pulse (130 fs), including the dynamics of the coherences. As a result, at 0 fs delay (corresponding to the pulse maximum) the anisotropy values are different for the secular and nonsecular cases (Figure 4). In the short pulse limit these initial values must be the same.

It is interesting that both our present study and that of ref 50 gave moderate differences between secular and nonsecular pictures for a multilevel system like B800 or B850 antenna. Notice in this respect that an earlier study of a dimer[60] showed larger nonsecular contributions.

Conclusions

We have studied the excitation dynamics in the B800−850 LH2 antenna using the Redfield theory approach for simultaneous and quantitative fitting of the experimental data. The latter includes linear spectra and two nonlinear kinetics, i.e., magic angle TA and anisotropy decays. Such a combination of two kinds of nonlinear spectroscopies sensitive to inter- and intraband transfers, respectively, is essential to obtain a self-consistent and more relevant picture of excitation dynamics. To obtain a realistic model, we used the full Redfield tensor in a basis of numerically calculated eigenstates (B800, B850, and B850* manifolds and mixed states). This gives us a rich picture with different relaxation channels including (i) intraband B800 → B800, B800 → B850*, B850* → B800, and B850* → B850* population transfers, (ii) interband B800 → B850 and B850* → B850 population transfers, (iii) intraband B850 → B850 population relaxation, (iv) dynamics of the coherences between one-exciton states from B800, B850, and B850* manifolds (with decay and transfer of the coherences), and (v) coupling between one-exciton populations and coherences due to nonsecular terms of the Redfield tensor. The resulting model of energy transfer is more complicated as compared with earlier models based on simplified approaches. Using this model, we adjusted the time scales of some channels, for example, B800 → B800 transfer was found to be 1 order of magnitude slower than in the previous schemes. On the other hand, our picture includes a lot of new relaxation channels (listed above), which were not considered by earlier models. Moreover, our modeling revealed that some kinetics components may have completely different physical origins as compared with their traditional assignment. Thus, we demonstrated that the fast subpicosecond component of anisotropy decay does not reflect any population migration at all but is connected with the coherence dynamics.

We conclude that our model of excitation dynamics in B800−850 antenna is different from the previous ones in some essential points, such as the ratio between intra-B800 and B800 → B850 migration, competition between different pathways of the B800 → B850 energy transfer (i.e., direct transfer and transfer through the B850* states), the existence of appreciable "detour" B850* → B800 channel, the nature of the B800 anisotropy decay. The main argument for such an alternative view is a possibility to obtain a good quantitative and simultaneous fit of the whole data set, that we really got and which was not possible so far.

Appendix A

The Redfield tensor elements needed to obtain the relaxation terms can be calculated as[58,59]

$$R_{ijkl} = -\langle v_{lj}v_{ik}\rangle(J_{jl} + J_{ik}) + \delta_{lj}\sum_s \langle v_{is}v_{sk}\rangle J_{sk} + \delta_{ik}\sum_s \langle v_{ls}v_{sj}\rangle J_{sl}$$

(A1)

where indexes i, j, k, l, and s denote the eigenstates of the system containing the ground-state g and the states from the one- and two-exciton manifolds and v_{ik} is the matrix element (in the eigenstate basis) of the system−bath interaction Hamiltonian, brackets indicating the averaging over the bath coordinates. The interaction Hamiltonians in the eigenstate (v) and site (v_s) representation are connected by the eigenfunction matrix $\mathbf{C}$ that diagonalize the system Hamiltonian, i.e., $v = \mathbf{C}^+ v_s \mathbf{C}$. The matrix element J_{ik} is the spectral density of the system−bath coupling. To account for intra- and interband transfers determined by coupling to low- and high-frequency modes, we need at least two-component spectral density, for example:

$$J_{kk'} = 4(1 - \delta_{kk'})\frac{V_1 W_1{}^2 \exp(-W_1) + V_2 W_2{}^2 \exp(-W_2)}{1 + \exp(\omega_{kk'}/k_B T)} +$$

$$\delta_{kk'}V_0$$

$$W_1 = |\frac{\omega_{kk'}}{\omega_{c1}}| \qquad W_2 = |\frac{\omega_{kk'}}{\omega_{c2}}| \qquad (A2)$$

where V_0 is the pure dephasing parameter, $k_B T$ is the temperature in the units of energy, $\omega_{kk'}$ is the energy splitting between exciton levels k and k', ω_{c1} and ω_{c2} are characteristic frequencies. Using this form, we got free parameters V_0, V_1, V_2, ω_{c1}, and ω_{c2} that must be adjusted from the fit.

Notice that eq A2 stems from the simplest form of the spectral density used in ref 25 for modeling of the B800 → B800 and B800 → B850 transfers. Using a stochastic model with correlation functions that decay exponentially and neglecting the frequency dependence of relaxation rates,[25,26,61] it is possible to obtain the frequency independent spectral density containing the same denominator as in eq A2 (see eq 9 in ref 61). The thus determined spectral density (as well as its generalized form, i.e., eq A2, where we introduced the frequency dependent factors W_1 and W_2) guarantees detailed balance at any fixed temperature. This is enough to study the dynamics at fixed temperature (as we do in this paper). Neither eq 9 in ref 61 nor our eq A2 predicts a correct temperature dependence of relaxation rates. To obtain a temperature-dependent Redfield tensor, more versatile representations of the spectral density[26,62,63] are needed.

Appendix B

Here we define the transfer rates, dipole strengths, and density of states shown in Figure 6. As we have seen in Table 1, the states in the 800 nm band are characterized by different participation of the BChl 800 and BChl 850 molecules. These participation values defined as

$$C_{800}(k) = \sum_n c_{nk}{}^2 \qquad n \in \{BChl800\}$$

$$C_{850}(k) = \sum_m c_{mk}{}^2 \qquad m \in \{BChl850\} \qquad (B1)$$

were found to be close to 1 or 0 (for all states with the exception of a few mixed states with equal participation values). It means that we can use these participation values to distinguish between B800 and B850* states in the 800 nm band (remind that the 850 nm band consists of B850 states with participation of the BChl's 850 only). The density of states with predominant participation of BChl's 800 or 850 is given by

$$S_{800}(\lambda) = \langle \sum_k C_{800}(k)\, L(\lambda - \lambda_k)\rangle$$

$$S_{850}(\lambda) = \langle \sum_k C_{850}(k)\, L(\lambda - \lambda_k)\rangle \qquad (B2)$$

where the L function gives a position (wavelength) of the kth state. This is a δ-function that can be replaced in numerical calculation by some finite width but not a sharp line shape function. Angular brackets denote an averaging over disorder. Figure 6 (left bottom) shows S_{800} and S_{850} in the 800 nm region (in the 850 nm region $S_{800} = 0$). The dipole strengths of B800, B850*, and B850 states are

$$D_{B800}(\lambda) = \langle \sum_{k=9}^{24} D_k C_{800}(k)\, L(\lambda - \lambda_k)\rangle S_{800}{}^{-1}(\lambda)$$

$$D_{B850*}(\lambda) = \langle \sum_{k=9}^{24} D_k C_{850}(k)\, L(\lambda - \lambda_k)\rangle S_{850}{}^{-1}(\lambda)$$

$$D_{B850}(\lambda) = \langle \sum_{k=1}^{8} D_k C_{850}(k)\, L(\lambda - \lambda_k)\rangle S_{850}{}^{-1}(\lambda) \qquad (B3)$$

where D_k is the dipole strength of the kth exciton state for one realization of the disorder. Averaging over disorder gives us the distribution shown in Figure 6 (right bottom). The transfer rates are defined as

$$k_{B800 \to B800}(\lambda) =$$
$$\langle \sum_{k=9}^{24} C_{800}(k) \sum_{k'=9}^{24} R_{kkk'k'} C_{800}(k')\, L(\lambda - \lambda_{k'})\rangle S_{800}{}^{-1}(\lambda)$$

$$k_{B800 \to B850*}(\lambda) =$$
$$\langle \sum_{k=9}^{24} C_{850}(k) \sum_{k'=9}^{24} R_{kkk'k'} C_{800}(k')\, L(\lambda - \lambda_{k'})\rangle S_{800}{}^{-1}(\lambda)$$

$$k_{B800 \to B850}(\lambda) =$$
$$\langle \sum_{k=1}^{8} C_{850}(k) \sum_{k'=9}^{24} R_{kkk'k'} C_{800}(k')\, L(\lambda - \lambda_{k'})\rangle S_{800}{}^{-1}(\lambda) \quad (B4)$$

$$k_{B850* \to B800}(\lambda) =$$
$$\langle \sum_{k=9}^{24} C_{800}(k) \sum_{k'=9}^{24} R_{kkk'k'} C_{850}(k')\, L(\lambda - \lambda_{k'})\rangle S_{850}{}^{-1}(\lambda)$$

$$k_{B850* \to B850*}(\lambda) =$$
$$\langle \sum_{k=9}^{24} C_{850}(k) \sum_{k'=9}^{24} R_{kkk'k'} C_{850}(k')\, L(\lambda - \lambda_{k'})\rangle S_{850}{}^{-1}(\lambda)$$

$$k_{B850* \to B850}(\lambda) =$$
$$\langle \sum_{k=1}^{8} C_{850}(k) \sum_{k'=9}^{24} R_{kkk'k'} C_{850}(k')\, L(\lambda - \lambda_{k'})\rangle S_{850}{}^{-1}(\lambda) \quad (B5)$$

$$k_{B850 \to B850}(\lambda) =$$
$$\langle \sum_{k=1}^{8} C_{850}(k) \sum_{k'=1}^{8} R_{kkk'k'} C_{850}(k')\, L(\lambda - \lambda_{k'})\rangle S_{850}{}^{-1}(\lambda) \quad (B6)$$

Here $R_{kkk'k'}$ is the Redfield tensor element describing a population transfer from the k'th to kth level (see Appendix A). By multiplying by $C_{800}(k')$ or $C_{850}(k')$ we select an initial state (i.e., only B800 in eq B4 or B850* in eq B5). We can also select a specific pathways (i.e., B800, B850* or B850 as a final state) by using $C_{800}(k)$ or $C_{850}(k)$ with summation over the states in an appropriate region. In our model, $1 < k < 8$ corresponds to 850 nm band, and $9 < k < 24$ to the 800 nm band. It is important that our participation values are determined through the square of the wave function amplitude (eq B1). Due to normalization of the eigenfunctions our rates are additive; i.e., the sum of the three rates in eq B4 or B5 gives us the total decay of the B800 or B850* states. These total decays (inverse lifetimes) are shown in Figure 6.

Appendix C

In this paper we calculated the transient absorption (TA) anisotropy using the third-order density martix equations together with the averaging-over-orientations rules for a polarized pump−probe.[33] Besides exact numerical solution (with arbitrary pulse duration and the full Redfield tensor) shown in Figure 4 it is useful to derive approximate analytical expressions to study the influence of different factors on the TA anisotropy. In this simple illustration we suppose narrow-band excitation and probe (corresponding to the stationary polarization limit), but we neglect relaxation during the pulse. We calculate sequential contributions only, and we restrict ourselves to a secular approximation for the Redfield tensor. The stimulated emission (SE), excited-state absorption (ESA), and photobleaching (PB) contributions can be then written in the form

$$SE = -\mathrm{Im}\{\sum_{k,k'}\rho_{kk'}d_k^{e_2}d_{k'}^{e_2}L_{kg}^{\omega_2}\}$$

$$L_{kg}^{\omega_2} = (\omega_{kg} - \omega_2 - iR_{kgkg})^{-1} \quad (C1)$$

$$ESA = \mathrm{Im}\{\sum_{k,k',q}\rho_{kk'}d_{qk}^{e_2}d_{qk'}^{e_2}L_{qk'}^{\omega_2}\}$$

$$L_{qk'}^{\omega_2} = (\omega_{qk'} - \omega_2 - iR_{qk'qk'})^{-1} \quad (C2)$$

$$PB = -\mathrm{Im}\{\sum_{k''}\rho_{k''k''}\sum_k d_k^{e_2}d_k^{e_2}L_{kg}^{\omega_2}\} \quad (C3)$$

where subscript indexes g, k, and q stand for ground, one- and two-exciton states, respectively. R_{kgkg} is the Redfield tensor elements giving a homogeneous broadening of the corresponding transitions, $\omega_{kg} = \omega_k - \omega_g$ is the transition frequency, d_k and d_{qk} are transition dipoles of one- and two-exciton transitions, superscript e_2 denotes a projection on the polarization vector of the probe, ω_2 is the probe frequency, and ρ_{kk} and $\rho_{k'k}$ denote the second-order one-exciton population and coherences, which are time-dependent with the initial values of

$$\rho_{kk'}(t{=}0) = id_k^{e_1}d_{k'}^{e_1}((L_{k'g}^{\omega_1})^* - L_{kg}^{\omega_1}) \quad (C4)$$

where superscript e_1 denotes a projection on the polarization vector of the pump and ω_1 is the pump frequency. The orientational averaging rules are

$$\langle a^{e_1}b^{e_1}c^{e_2}d^{e_2}\rangle_{\|-\perp} = \frac{1}{30}[-2(\mathbf{ab})(\mathbf{cd}) + 3(\mathbf{ac})(\mathbf{bd}) + 3(\mathbf{ad})(\mathbf{bc})]$$

$$\langle a^{e_1}b^{e_1}c^{e_2}d^{e_2}\rangle_{\|+2\perp} = \frac{1}{3}(\mathbf{ab})(\mathbf{cd}) \quad (C5)$$

Supposing that the exciton components are broader than the

splitting between them (see 800 nm region in Figure 1), we can obtain the SE anisotropy arising from the coherent excitation of the two levels, k and k':

$$r_{\mathrm{in}}^{\mathrm{SE}} = \frac{2d_k^4 + 2d_{k'}^4 + [3d_k^2d_{k'}^2 + (\mathbf{d}_k\mathbf{d}_{k'})^2]e^{-R_{kk'kk'}t}\cos(\omega_{kk'}t)}{5d_k^4 + 5d_{k'}^4 + 10(\mathbf{d}_k\mathbf{d}_{k'})^2e^{-R_{kk'kk'}t}\cos(\omega_{kk'}t)}$$

$$r_{\mathrm{eq}}^{\mathrm{SE}} = \frac{2d_k^4 + 2d_{k'}^4 - 2d_k^2d_{k'}^2 + 6(\mathbf{d}_k\mathbf{d}_{k'})^2}{5d_k^4 + 5d_{k'}^4 + 10d_k^2d_{k'}^2} \quad (C6)$$

where r_{in} corresponds to anisotropy dynamics prior to population transfer including coherence decay only. This is aperiodic decay, almost purely exponential, because we supposed that $R_{kk'kk'} \gg \omega_{kk'}$. The anisotropy after population equilibration is r_{eq}, where we supposed that $\rho_{kk} = \rho_{k'k'}$ in equilibrium. If transition dipoles are perpendicular to each other and have equal values, we got depolarization from $r_{\mathrm{in}} = 0.7$ at $t = 0$ to $r_{\mathrm{in}} = 0.4$ at $t \to \infty$ due to coherence decay. Population equilibration leads to $r_{\mathrm{eq}} = 0.1$. The corresponding PB anisotropy is time-independent:

$$r_{\mathrm{in}}^{\mathrm{PB}} = r_{\mathrm{eq}}^{\mathrm{PB}} = \frac{2d_k^4 + 2d_{k'}^4 - 2d_k^2d_{k'}^2 + 6(\mathbf{d}_k\mathbf{d}_{k'})^2}{5d_k^4 + 5d_{k'}^4 + 10d_k^2d_{k'}^2} \quad (C7)$$

giving $r = 0.1$ for equal dipoles with perpendicular orientaiton. Far from two-exciton resonances a combined SE + PB contribution gives $0.3 \to 0.2$ and $0.2 \to 0.1$ anisotropies during coherence and population decay periods instead of $0.7 \to 0.4$ and $0.4 \to 0.1$ values for a pure SE.

The ESA component (depending on one- to two-exciton transition dipoles d_{qk}) typically gives the initial values of $r_{\mathrm{in}} = 0.25-0.35$ ($t = 0$) with subsequent depolarization to $r_{\mathrm{in}} = 0.15-0.25$ due to coherence decay and further depolarization to $r_{\mathrm{eq}} = 0.06-0.1$ due to population equilibration. Thus, the resulting SE + PB + ESA anisotropy shows the initial (coherent) values of about $0.3-0.35$, the incoherent values of $0.15-0.25$, and thermalized values close to 0.1.

References and Notes

(1) McDermott, G.; Prince, S. M.; Freer, A. A.; Hawthornthwaite-Lawless, A. M.; Papiz, M. Z.; Cogdell, R. J.; Isaacs, N. W. *Nature* **1995**, *374*, 517.

(2) Koepke, J.; Hu, X.; Muenke, C.; Schulten, K.; Michel, H. *Structure* **1996**, *4*, 581.

(3) Sundström, V.; Pullerits, T.; van Grondelle, R. *J. Phys. Chem. B* **1999**, *103*, 2327.

(4) van Grondelle, R.; Novoderezhkin, V. *Biochemistry* **2001**, *40*, 15057.

(5) Hu, X.; Ritz, T.; Damjanović, A.; Autenrieth, F.; Schulten, K. *Q. Rev. Biophys.* **2002**, *35*, 1.

(6) van der Laan, H.; Schmidt, Th.; Visschers, R. W.; Visscher, K. J.; van Grondelle, R.; Völker, S. *Chem. Phys. Lett.* **1990**, *170*, 231.

(7) Reddy, N. R. S.; Small, G. J.; Seibert, M.; Picorel, R. *Chem. Phys. Lett.* **1991**, *181*, 391.

(8) de Caro, C. D.; Visschers, R. W.; van Grondelle, R.; Völker, S. *J. Phys. Chem.* **1994**, *98*, 10584.

(9) Wu, H.-M.; Savikhin, S.; Reddy, N. R. S.; Jankowiak, R.; Cogdell, R. J.; Small, G. J. *J. Phys. Chem.* **1996**, *100*, 12022.

(10) Matsuzaki, S.; Zazubovich, V.; Fraser, N. J.; Cogdell, R. J.; Small, G. J. *J. Phys. Chem. B* **2001**, *105*, 7049.

(11) Zazubovich, V.; Jankowiak, R, Small, G. J. *J. Lumin.* **2002**, *98*, 123.

(12) Hess, S.; Feldchtein, F.; Babin, A.; Nurgaleev, I.; Pullerits, T.; Sergeev, A.; Sundström, V. *Chem. Phys. Lett.* **1993**, *216*, 247.

(13) Hess, S.; Åkesson, E.; Cogdell, R. J.; Pullerits, T.; Sundström, V. *Biophys. J.* **1995**, *69*, 2211.

(14) Monshouwer, R.; Ortiz de Zarate, I.; van Mourik, F.; van Grondelle, R. *Chem. Phys. Lett.* **1995**, *246*, 341.

(15) Joo, T.; Jia, Y.; Yu, J.-Y.; Jonas, D. M.; Fleming, G. R. *J. Phys. Chem.* **1996**, *100*, 2399.

(16) Ma, Y. Z.; Cogdell, R. J.; Gillbro, T. *J. Phys. Chem. B* **1997**, *101*, 1087.

(17) Ma, Y. Z.; Cogdell, R. J.; Gillbro, T. *J. Phys. Chem. B* **1998**, *102*, 881.

(18) Kennis, J. T. M.; Streltsov, A. M.; Aartsma, T. J.; Nozava, T.; Amesz, J. *J. Phys. Chem.* **1996**, *100*, 2438.

(19) Kennis, J. T. M.; Streltsov, A. M.; Vulto, S. I. E.; Aartsma, T. J.; Nozava, T.; Amesz, J. *J. Phys. Chem. B* **1997**, *101*, 7827.

(20) Pullerits, T.; Hess, S.; Herek, J. L.; Sundström, V. *J. Phys. Chem. B* **1997**, *101*, 10560.

(21) Ihalainen, J. A.; Linnanto, J.; Myllyperkiö, P.; van Stokkum, I. H. M.; Ücker, B.; Scheer, H.; Korppi-Tommola, J. E. I. *J. Phys. Chem. B* **2001**, *105*, 9849.

(22) Wendling, M.; van Mourik, F.; van Stokkum, I. H. M.; Salverda, J. M.; Michel, H.; van Grondelle, R. *Biophys. J.* **2003**, *84*, 440.

(23) Salverda, J. M.; van Mourik, F.; van der Zwan, G.; van Grondelle, R. *J. Phys. Chem. B* **2000**, *104*, 11395.

(24) Agarwal, R.; Yang, M.; Xu, Q. H.; Fleming, G. R. *J. Phys. Chem. B* **2001**, *105*, 1887.

(25) Kühn, O.; Sundström, V. *J. Phys. Chem. B* **1997**, *101*, 3432.

(26) Renger, Th.; May, V.; Kühn, O. *Phys. Rep.* **2001**, *343,* 137.

(27) Herek, J. L.; Fraser, N. J.; Pullerits, T.; Martinsson, P.; Polívka, P.; Scheer, H.; Cogdell, R. J.; Sundström, V. *Biophys. J.* **2000**, *78*, 2590.

(28) Mukai, K.; Abe, S.; Sumi, H. *J. Phys. Chem. B* **1999**, *103*, 6096.

(29) Scholes, G. D.; Fleming, G. R. *J. Phys. Chem. B* **2000**, *104*, 1854.

(30) Yang, M.; Fleming, G. R. *Chem. Phys.* **2002**, *275*, 355.

(31) Zhang, W. M.; Meier, T.; Chernyak, V.; Mukamel, S. *J. Chem. Phys.* **1998**, *108*, 7763.

(32) Kühn, O.; Sundström, V. *J. Chem. Phys.* **1997**, *107*, 4154.

(33) Novoderezhkin, V.; van Grondelle, R. *J. Phys. Chem. B* **2002**, *106*, 6025.

(34) Wendling, M.; Pullerits, T.; Przyjalgowski, M. A.; Vulto, S. I. E.; Aartsma, T. J.; van Grondelle, R.; van Amerongen, H. *J. Phys. Chem. B* **2000**, *104*, 5825.

(35) Damjanović, A.; Kosztin, I.; Kleinekathöfer, U.; Schulten, K. *Phys. Rev. E* **2002**, *65*, 031919.

(36) Gillie, J. K.; Small, G. J.; Goldbeck, J. H. *J. Phys. Chem.* **1989**, *93*, 1620.

(37) Zazubovich, V.; Matsuzaki, S.; Johnson, T. W.; Hayes, J. M.; Chitnis, P. R.; Small, G. J. *Chem. Phys.* **2002**, *275*, 47.

(38) Beekman, L. M. P.; Frese, R. N.; Fowler, G. J. S.; Picorel, R.; Cogdell, R. J.; van Stokkum, I. H. M.; Hunter, C. N.; van Grondelle, R. *J. Phys. Chem. B* **1997**, *101*, 7293.

(39) Beekman, L. M. P.; Steffen, M.; van Stokkum, I. H. M.; Olsen, J. D.; Hunter, C. N.; Boxer, S. J.; van Grondelle, R. *J. Phys. Chem. B* **1997**, *101*, 7284.

(40) Somsen, O. J. G.; Chernyak, V.; Frese, R. N.; van Grondelle, R.; Mukamel, S. *J. Phys. Chem. B* **1998**, *102*, 8893.

(41) Monshouwer, R.; Abrahamsson, M.; van Mourik, F.; van Grondelle, R. *J. Phys. Chem. B* **1997**, *101*, 7241.

(42) Knox, R. S.; Gülen, D. *Photochem. Photobiol.* **1993**, *57*, 40.

(43) Kumble, R.; Palese, S.; Visschers, R. W.; Dutton, P. L.; Hochstrasser, R. M. *Chem. Phys. Lett.* **1996**, *261*, 396.

(44) Arnett, D. C.; Moser, C. C.; Dutton, P. L.; Scherer, N. F. *J. Phys. Chem. B* **1999**, *103*, 2014.

(45) Meier, T.; Chernyak, V.; Mukamel, S. *J. Phys. Chem. B* **1997**, *101*, 7332.

(46) van Grondelle, R.; Kramer, H. J. M.; Rijgersberg, C. P. *Biochim. Biophys. Acta* **1982**, *682*, 208.

(47) Wynne, K.; Hochstrasser, R. M. *Chem. Phys.* **1993**, *171*, 179.

(48) Matro, A.; Cina, J. A. *J. Phys. Chem.* **1995**, *99*, 2568.

(49) Kumble, R.; Hochstrasser, R. M. *J. Chem. Phys.* **1998**, *109*, 855.

(50) Kühn, O.; Sundström, V.; Pullerits, T. *Chem. Phys.* **2002**, *275*, 15.

(51) Bradforth, S. E.; Jimenez, R.; van Mourik, F.; van Grondelle, R.; Fleming, G. R. *J. Phys. Chem.* **1995**, *99*, 16179.

(52) Jimenez, R.; Dikshit, S. N.; Bradforth, S. E.; Fleming, G. R. *J. Phys. Chem.* **1996**, *100*, 6825.

(53) Nagarajan, V.; Alden, R. G.; Williams, J. C.; Parson, W. W. *Proc. Natl. Acad. Sci. U.S.A.* **1996**, *93*, 13774.

(54) Nagarajan, V.; Johnson, E. T.; Williams, J. C.; Parson, W. W. *J. Phys. Chem. B* **1999**, *103*, 2297.

(55) Chachisvilis, M.; Kühn, O.; Pullerits, T.; Sundström, V. *J. Phys. Chem. B* **1997**, *101*, 7275.

(56) Monshouwer, R.; Baltuška, A.; van Mourik, F.; van Grondelle, R. *J. Phys. Chem. A* **1998**, *102*, 4360.

(57) Vulto, S. I. E.; Kennis, J. T. M.; Streltsov, A. M.; Amesz, J.; Aartsma, T. J. *J. Phys. Chem. B* **1999**, *103*, 878.

(58) Redfield, A. G. *Adv. Magn. Reson.* **1965**, *1*, 1.

(59) Pollard, W. T.; Felts, A. K.; Friesner, R. A. *Adv. Chem. Phys.* **1996**, *93*, 77.

(60) Čápek, V.; Barvík, I.; Heřman, P. *Chem. Phys.* **2001**, *270*, 141.

(61) Jean, J. M.; Fleming, G. R. *J. Chem. Phys.* **1995**, *103*, 2092.

(62) Renger, T.; Marcus, R. A. *J. Chem. Phys.* **2002**, *116*, 9997.

(63) Chernyak, V.; Minami, T.; Mukamel, S. *J. Chem. Phys.* **2000**, *112*, 7953.